福井大学審査

学位論文［博士（工学)］

（A Dissertation Submitted to the
University of Fukui for the Degree of
Doctor of Engineering）

Real-time 3D Visualization and Navigation Using Line Laser and Optical Fiber Applied to Narrow Space

ラインレーザと光学ファイバーを用いた極小領域における リアルタイム三次元可視化とナビゲーション

2016 September

Zhongjie Long
龍　忠傑

UNIVERSITY OF FUKUI

Abstract

Department of Advanced Interdisciplinary Science and Technology

Doctor of Engineering

Real-time 3D Visualization and Navigation Using Line Laser and Optical Fiber Applied to Narrow Space

by Zhongjie LONG

Minimally invasive surgery is a popular technique that uses an endoscopic camera for direct viewing of patients' internal organs for diagnosis and treatment. The use of this technique is increasingly performed at current clinical applications because it has advantages over the open surgery in terms of less trauma and faster recoveries. However, conventional endoscope-based surgery does not provide stereoscopic information to the surgeon. Accordingly, surgeons can only view the operation field via a video monitor on which two-dimensional information of the surgical target are displayed. To overcome this limitation, an endoscopic system was developed for visualizing the knee joint surface and navigating its normal vector in real-time.

The endoscopic system is composed of an endoscopic camera, line laser, optical fiber and acrylic prism. Two versions of the system configuration were specifically designed based on the baseline and tested in experimental studies.

It is a challenge that the dimension of the endoscope can not be increased beyond 8 mm for practical applications in real surgery. Therefore, using the optical fiber and prism ensured a relatively long baseline while maintaining the small diameter of the endoscope. Meanwhile, an endoscopic tube was developed for a special diameter in order to apply in narrow space.

Without using a specific vertex configuration algorithm, the point cloud obtained by the current endoscopic system is unable to render and thus isosurface can not be extracted. Hence, we proposed a modified marching cubes algorithm for the vertex processing. This method arranges the spatial points using midpoint comparison to construct three-dimensional regular grids. The experimental results demonstrated that the extracted surface is able to render and the cubic interval being 1.27 mm can obtain a smooth rendering surface. Further, a comparison results showed that the proposed marching cubes did not change the accuracy of the reconstructed surface.

Two sets of stereo reconstruction experiments were performed using system I and system II respectively. The first set using a camera of 7.0 mm diameter was tested in air. It focuses on investigating the correlation between the baseline and the reconstructed accuracy. The results revealed that the quality of laser point detection improved when the deviation angle of the line laser with respect to the optical axis was 14° in case that the baseline was 6 mm. Based on the results, it was assumed that the deviation angle of the line laser could be achieved by using a prism. The second set was conducted using a 3.9 mm diameter camera in the water. Reconstruction of planar surface revealed that current system has an average measurement error of 0.54 mm with the mean of standard deviation (SD) being 0.26 mm. A comparative method using the least squares fitting was employed to assess the accuracy of the surface reconstruction. The results showed an average error of 2.42 mm that corresponded to a difference of 4.93% from the ideal diameter; assuming those of the knee joint surface are the same.

In navigation experiments, as the second goal of our study, a specific navigation approach suitable for use in a rendered surface was presented in extenso.

An experiment of navigating a normal vector using a femoral bone was performed under water. Each location of the rendering surface can be navigated by the harvester and displayed on the graphical user interface, the surgeon can easily adjust the pose of the instrumentation based on the displayed navigation info. The experimental results show that our system has an average navigation error of 9.5° within the range of 5° to 17°, with an SD of 2.86°. In contrast, the errors for two sites when applying a freehand technique during arthroscopic surgery were 14.8° within the range of 6° to 26° (SD of 7.53°), and 12.6° within the range of 4° to 17° (SD of 3.98°). A statistical analysis showed a significant difference ($P = 0.001$ and $P = 0.0024$) between the navigated technique (N = 30) and freehand technique (N = 20).

In conclusion, we have developed a fiber-based endoscopic system that enable small surface in narrow space to be visualized and navigated. Surgeons will be able to identify and locate the surgical tool based on the displayed tips, which will assist in their decision making. The small diameter (8 mm) of our endoscope makes it extremely convenient for potential application in an arthroscopic surgery.

Acknowledgements

The single life of being a student in a foreign country is a bittersweet memory that will never be forgotten. Throughout three years in Japan, I gained a lot of knowledge not only limited to my research, but also invaluable experiences that have made me the person I am today.

First and foremost, I would like to express my special appreciation and thanks to my advisor Prof. Dr. Kouki Nagamune, he has been a tremendous mentor for me. His advice on both research as well as on my career has been priceless. I would also like to thank Prof. Dr. Kazuyuki Murase for giving me the opportunity to conduct this research. I also want to thank Shogo Kawaguchi, Feng Zhang, and Yusuke Shimizu, who helps in providing the materials of the experiment, and Mohd Hanafi, Muhammad Khairul, Yosuke Uozumi, and all laboratory members for their insightful comments and encouragement.

My gratitude to Prof. Masahiro Kurosaka, Prof. Ryosuke Kuroda, Dr. Tomoyuki Matsushita, Dr. Daisuke Araki, and Dr. Yuichi Hoshino of Graduate School of Medicine, Kobe University, Japan for providing materials and useful discussion throughout this work.

Financially, this work was supported by a Grant-in-Aid for Young Scientists (B) (No. 25870273) from the Ministry of Education, Culture, Science, and Technology of Japan. My sincere thanks also go to Prof. Dr. Xiaoli Xu of Beijing Information Science & Technology University for providing utmost support to my abroad study.

Last but not least, a million thanks to my beloved parents and my younger brother, who continually supported me in writing this thesis, and incented me to strive towards my goal.

Zhongjie Long
Feb. 16, 2016, Fukui Japan

Contents

List of Figures

List of Tables

List of Abbreviations

2D	**T**wo **D**imensional
3D	**T**hree **D**imensional
API	**A**pplication **P**rogram **I**nterface
CAS	**C**omputer **A**ssisted **S**urgical
CMC	**C**lassical **M**arching **C**ubes
CT	**C**omputed **T**omography
DoF	**D**egree **o**f **F**reedom
GUI	**G**raphical **U**ser **I**nterface
IPC	**I**nter **P**rocess **C**ommunication
IVR	**I**ndirect **V**olume **R**endering
LSF	**L**east **S**quares **F**itting
MIS	**M**inimally **I**nvasive **S**urgery
MRI	**M**agnetic **R**esonance **I**maging
OAT	**O**steochondral **A**utologous **T**ransplantation
PMC	**P**roposed **M**arching **C**ubes
RMS	**R**oot **M**ean **S**quare
SD	**S**tandard **D**eviation

Chapter 1

Introduction

Osteochondral transplantation is not a new technique. Over the past 70 years, there have been numbers of reports on the use of allograft and autogenous osteochondral material for the treatment of osteochondritis dissecans and for replacement of bone defects after tumor resection [1]. Since the Mosaicplasty method was proposed, there have been several clinical applications [2]–[4] on the use of cylindrical osteochondral autografts for the treatment of focal chondral and femoral condylar defects in the knee.

Femoral condylar defects can be treated arthroscopically or by open technique in terms of its size. Smaller lesions, less than 1.5 cm in diameter, can be proceed arthroscopically [1]. Special arthroscopic instrumentations were developed for obtaining and inserting the plugs. Nevertheless, the operation of the instrumentation relies mainly on the surgeon's level of experience.

As the optical technique has grown, computer-assisted surgical (CAS) system allows for more precise localization or navigation information of the instrumentation. However, standard endoscopes adopted in a clinical application are not equipped with any global position tracking device to provide camera's location and orientation. Hence, recovering depth information of the surgical objects in minimally invasive surgery (MIS) is crucial for developing advanced image-guided and navigation systems [5]. Since the last decade, various CAS systems that provide real-time stereo vision or navigation during diagnoses or surgery have been increasingly developed. Some recent works utilized external intraoperative markers for the tracking of pose estimation [6], [7]. Other works do not require any markers have been developed most recently. Depth-from-Intensity method [8] was presented and used for 3D reconstruction of virtual colon structure without any global positioning device. Similarly, an adaptive marker-free registration approach has been successfully performed to provide real-time endoscope electromagnetic navigation [9]. A novel technique that simultaneously segment multi-structure in multiple views of endoscopic videos has been proposed by [10]. The 3D pose of the preoperative model can be automatically estimated and tracked. However, currently, there is a very limited number of CAS system available on navigation performing in the knee during osteochondral transplantation.

1.1 Objectives

The goal of this research is twofold. On one hand, it focuses on developing a real-time endoscopic system for reconstructing the surface of the object in narrow operating filed. The ability of the system to visualize surgical objects will be expected to improve the operating precision.

On the other hand, it attempts to navigate a normal vector of the recovered surface using the developed system. The normal direction corresponding to the current point can be determined, thus contributing a low-cost alternative for the real-time assistant analysis. The current system can be used as a stepping stone for further study in the near future. Figure 1.1 depicts the goals above using a block diagram.

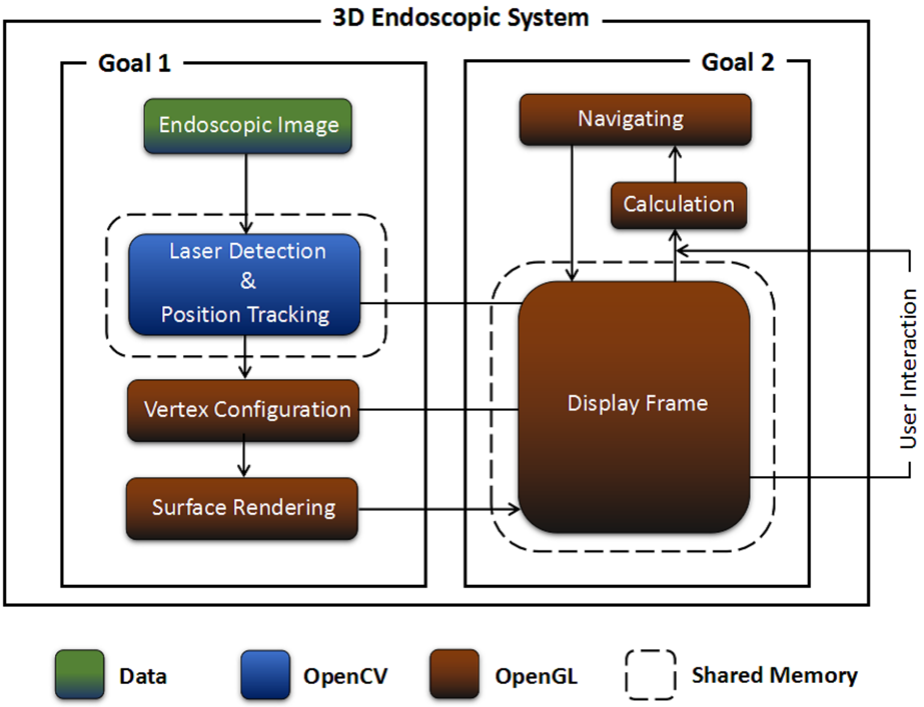

FIGURE 1.1: A simplified block diagram of our endoscopic system. The arrow indicates the process step, and the line indicates that data will be loaded into the display unit automatically when its corresponding process is finished.

1.2 Thesis Structure

This thesis is composed of six chapters and organized as follows.

In Chapter 1, a very brief introduction of the research background is presented. The research objectives and steps are highlighted, followed by explanation on the layout of this thesis. Chapter 2 describes the problem of osteochondral lesions in the knee and its treatment method. Chapter 3 introduces the component design, the adopted devices, and the system graphical user interface. Chapter 4 explains the proposed method of the stereo reconstruction, followed by experiments with system I and system II. Navigation approach and corresponding results are presented in Chapter 5. Finally, Chapter 6 summarizes the research findings and possible improvements of the current endoscopic system.

Chapter 2

Background Study

2.1 Osteochondral Lesions of the Knee

Osteochondral lesions of the knee are not uncommon in athletic individuals, typically the result of osteochondritis dissecans or trauma [11]. Individuals with this injury may suffer from swelling, pain, joint effusion, synovitis and early degenerative changes [12]–[15].

The impacts of osteochondral lesions in our life cannot be underestimated. Crul *et al.* reviewed 31,516 knee arthroscopies performed within four years of 1990's, and 53,569 hyaline cartilage lesions were documented in 19,827 patients, in which osteochondral lesions were the majority [16]. Widuchowski *et al.* found that osteochondral lesions were happened in 60% of the patients, according to their analysis of 25,124 knee arthroscopies performed from 1989 to 2004 [17]. Physical activity with an increase in sports participation in all age groups is responsible for the growing incidence of these lesions [18].

2.2 Osteochondral Autograft Transplantation and It's Procedure

To date, there are multiple techniques proposed to address osteochondral lesions. For example, micro-fracture, osteochondral allograft transplantation [19]–[21], autologous chondrocytes implantation [22]–[25], and osteochondral autologous transplantation (OAT) [26]–[28].

OAT is a reconstructive surgical procedure that addresses osteochondral lesions while maintaining the hyaline cartilage by replacing defect area with single osteochondral autograft [29]. As illustrated in Fig. 2.1, cylindrical osteochondral plug is harvested from a low-weight-bearing area of the femur and then injected into the defect region.

The Mosaicplasty method, firstly proposed by Hangody *et al.*, was conceived in the early 1990's. In this method, multiple small cylindrical plugs can be transfered to the regions with great-weight-bearing through an arthroscopic approach. Since then, Mosaicplasty has been used widely for the treatment of osteochondral lesions, particularly for smaller full-thickness chondral defects [11], [18], [30].

According to the study reported by M. Mark *et al.* in 2008 [31], mainly procedure of the OAT is divided into six steps:

Step 1: Diagnostic arthroscopy.
After establishing the arthroscopic portals, a systematic evaluation is performed for all compartments of the knee. Any loose bodies, as well as a small portion of the fat pad, should be removed to facilitate visualization of the lesion area.

Step 2: Graft harvest at the donor site.
The graft-harvesting extractor is driven into the subchondral bone to a depth of 10-15 mm. The graft is then removed perpendicularly from the low-weight-bearing zone by rotating the T-handle by 90° twice, clockwise and then counterclockwise.

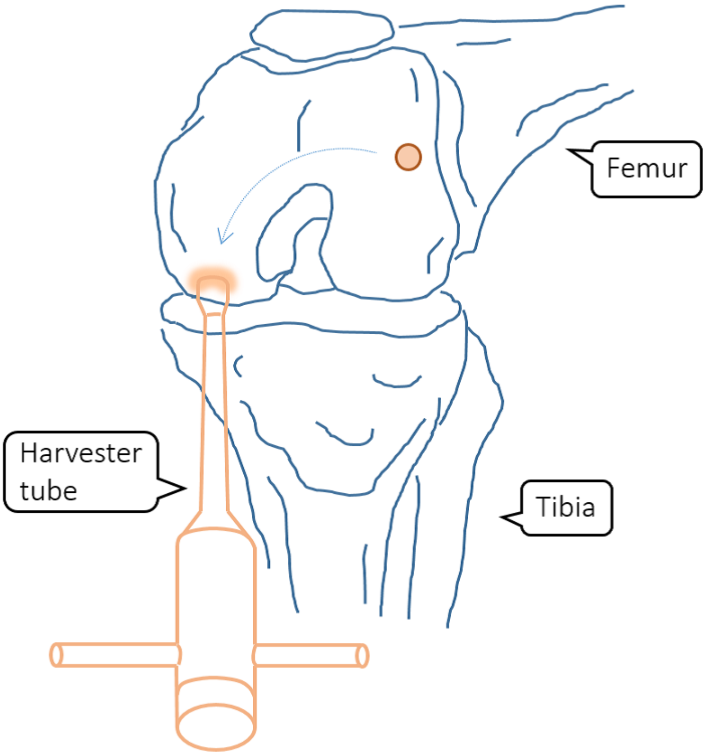

FIGURE 2.1: Schematic representation of the OAT.

Step 3: Backfilling the donor plug.

The donor plug is backfilled with a synthetic plug.

Step 4: Preparing the recipient site.

The recipient tool is placed at an angle of 90° to the lesion area.

Step 5: Graft placement.

Using a tamp, the osteochondral graft is gently inserted into the recipient socket.

Step 6: Closure.

Arthrotomy incisions are closed in layers.

In fact, surgical procedure of the OAT is not an easy task, numerous papers have been carried out to elucidate the critical reasons for difficulties in a variety

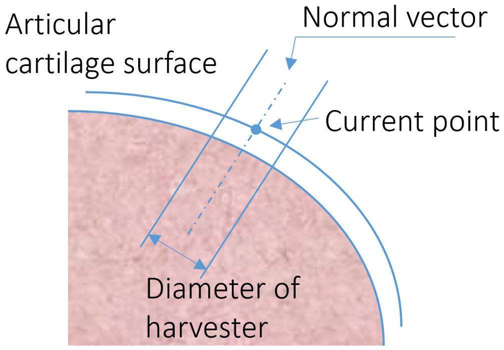

FIGURE 2.2: Graft harvesting and inserting on the joint surface using a harvester.

of aspects. For example, D. Koulalis *et al.* [32] have reported that factors affecting the accuracy of trimming of knee joint cartilage surface include the angle of the harvesting tube and resultant depth graft insertion. Refs. [31], [33]–[36] suggested that both grafts harvest and insertion have to be performed at 90° to the articular surface of the femoral condyle. In other words, one of the crucial steps during an OAT surgery is for the surgeons to decide the optimal pose of the instrumentation. Fig. 2.2 illustrates perpendicularly harvesting/inserting an autologous osteochondral plugs in relation to the articular cartilage surface. The normal vector indicates the central axis of the harvester tube.

Tow clinical studies, [4] and [37] emphasized that accuracy of grafts harvest had been identified as a major factor of success in OAT. Furthermore, several medical technical factors play a critical role in the success of this surgery, such as the overall surface coverage [38], the size [30] and shape [39] of the osreochondral grafts, and congruency of the articular cartilage surface of the knee between recipient and donor site [14].

Chapter 3

Design of the Components and System

3.1 Introduction

In this chapter, the design of the components is described. Meanwhile, the devices and instruments adopted in our research are also introduced.

3.2 Camera I and II

In our research, two cameras with different size were employed. The first one with 7.0 mm diameter was used for experiments in air, and the second one with 3.9 mm diameter was used for underwater experiments. Corresponding experiments will be described later in Chapter 4. Table 3.1 below summarizes the parameters of the two cameras.

3.2.1 Calibration

Calibration for the camera is to determine the intrinsic matrix, extrinsic matrix, and distortion coefficients, which is essential prior to the 3D measurement.

For a pinhole model, the most successful model, the relationship between the 3D world coordinate of a physical point $S = [x_w, y_w, z_w]^T$ and its corresponding coordinates $s = [u, v]^T$ projected on the image plane can be described

TABLE 3.1: Camera parameters.

Items	Camera I	Camera II
Product model	T&J TM-7M-USB-E	M244P-T0833W-105-L
Image sensor	1/6" CMOS	1/18" CMOS
Dimension	ϕ 7 mm × 40 mm	ϕ 3.9 mm × 15 mm
Effective pixel	640 × 480 pixels	320 × 240 pixels
Angle of view	54 degrees	105 degrees
Focus distance	60 mm - infinite	20 mm - infinite
Waterproof	Yes	Yes
LED brightness	adjustable	unadjustable

as follows [40], [41]

$$\lambda \begin{bmatrix} s \\ 1 \end{bmatrix} = \boldsymbol{M} \begin{bmatrix} \boldsymbol{R}_c & \boldsymbol{T}_c \end{bmatrix} \begin{bmatrix} S \\ 1 \end{bmatrix}, \tag{3.1}$$

where λ is a scale factor, $[\boldsymbol{R_c}\ \boldsymbol{T_c}]$ indicates the extrinsic matrix with $\boldsymbol{R_c}$ the rotation matrix, and $\boldsymbol{T_c}$ the translation vector.

$$\boldsymbol{M} = \begin{bmatrix} \alpha & \eta & u_o \\ 0 & \beta & v_o \\ 0 & 0 & 1 \end{bmatrix}, \tag{3.2}$$

denotes the intrinsic matrix with α and β are the focal lengths in pixel unit along the horizontal and vertical axes, η is the skew factor, and (u_o, v_o) represents the coordinates of the principle point.

There are two main distortions in a lens, that is radial distortion and tangential distortion. The distortion coefficients are given as

$$d_c = [r_1, r_2, t_1, t_2], \tag{3.3}$$

where r_1, r_2 indicate the radial distortion coefficients, and t_1, t_2 indicate the tangential distortion coefficients.

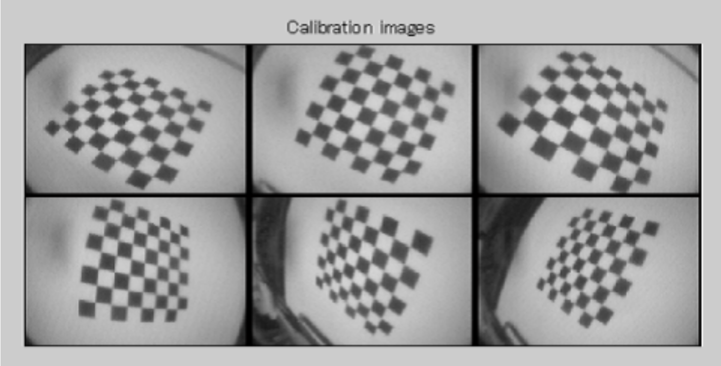

FIGURE 3.1: Images used for camera calibration.

3.2.2 Results

Camera calibration was performed using the method [42] developed by J. Y. Bouguet. By analyzing 6 images took by the camera I with different view angles (Fig. 3.1), intrinsic and extrinsic parameters of the camera could be automatically obtained in Matlab (The MathWorks, Inc., USA).

Calibration results of the camera I are

$$\boldsymbol{M}^{I} = \begin{bmatrix} 771.3048 & 0 & 319.5000 \\ 0 & 711.3048 & 239.5000 \\ 0 & 0 & 1 \end{bmatrix},$$

$$d_c^I = \begin{bmatrix} 0.1852 & -0.8874 & 0.0043 & -0.0069 \end{bmatrix},$$

$$\boldsymbol{R}_{\mathbf{c}}^{I} = \begin{bmatrix} 0.2090 & 0.9243 & 0.3195 \\ 0.7948 & 0.0298 & -0.6061 \\ -0.5697 & 0.3806 & -0.7284 \end{bmatrix},$$

$$\boldsymbol{T}_{\mathbf{c}}^{I} = \begin{bmatrix} -102.0203 & -78.4741 & 364.3632 \end{bmatrix}^T,$$

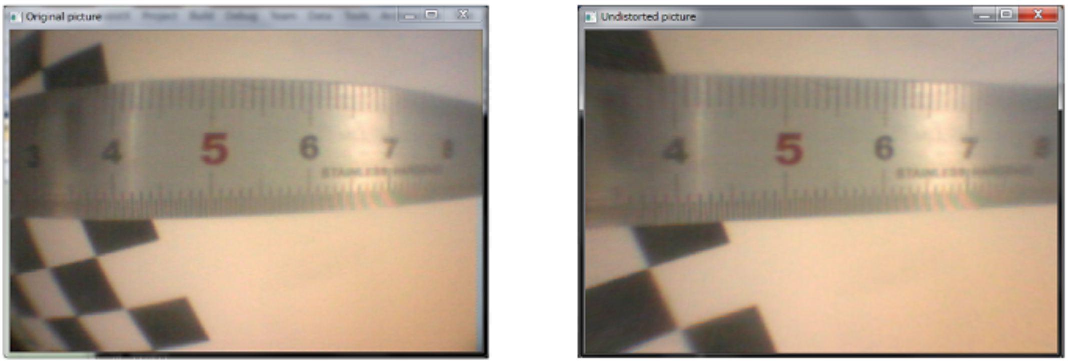

(a) (b)

FIGURE 3.2: Image difference: (a) before undistortion, and (b) after undistortion.

Using the same procedure, we can obtain the parameters of the camera II as follows

$$\boldsymbol{M}^{II} = \begin{bmatrix} 609.9614 & 0 & 359.5034 \\ 0 & 609.9623 & 239.4773 \\ 0 & 0 & 1 \end{bmatrix},$$

$$d_c^{II} = \begin{bmatrix} -0.3579 & -0.2402 & -0.0197 & 0.0188 \end{bmatrix},$$

$$\boldsymbol{R}_{\mathbf{c}}^{II} = \begin{bmatrix} -0.7253 & 0.6650 & -0.1783 \\ 0.6798 & 0.6510 & -0.3377 \\ -0.1085 & -0.3662 & -0.9242 \end{bmatrix},$$

$$\boldsymbol{T}_{\mathbf{c}}^{II} = \begin{bmatrix} 28.5271 & -166.0113 & 497.0222 \end{bmatrix}^T.$$

OpenCV provides us with a ready-to-use undistortion algorithm. Based on the distortion coefficients, raw image sequence can be corrected. For example, one frame of the raw image sequence was captured and displayed in Fig. 3.2(a), and Fig. 3.2(b) shows the undistorted result of Fig. 3.2(a) after camera calibration.

FIGURE 3.3: Photograph of the optical fiber.

TABLE 3.2: Structure parameters of the fiber scope.

Items	Details
Product model	SPN-09
Diameter of lens	15 mm
Diameter of fiber	0.9 mm ± 0.1 mm
Resolution of lens	7,400 pixels
Angle of view	50 degrees

3.3 Optical Fiber

In order to scale down the size of the endoscope, an optical fiber, one side of the fiber scope, was used for the irradiation of the line laser. Fig. 3.3 shows the fiber scope's structure (Asahi Kasei Corp., Japan). The side with the lens was attached to a laser projector and thus, the line laser can be transmitted through the optical fiber. More detailed parameters are given in Table 3.2.

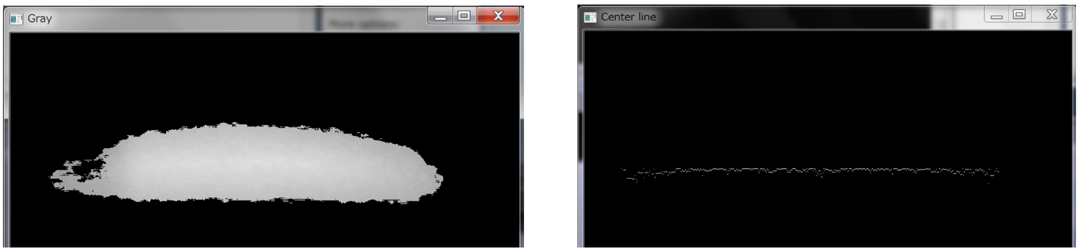

(a) Extracted area from the initial image.

(b) Central coordinates of the line laser.

FIGURE 3.4: Segmentation of the line laser.

3.4 Line Laser

Structured light techniques that use an artificial pattern of light are able to recover the 3D surface of an object. The principle is based on parallax and the trigonometric relationship generated between the projection center and a single camera.

In our system, line laser was yielded by a laser projector and projected onto the surface of an object. The line laser can be segmented using image processing technique which depends on its color values (red, green, and blue), see Fig. 3.4(a). Central coordinates of the illuminated area were computed based on the weighted average of the laser intensity. Extracted results are shown in Fig. 3.4(b).

3.5 Component Design

3.5.1 Prism

The design of the prism was based on the properties of the endoscope and light projector. Taking into account the fact that objects closer to the endoscope tip have a larger parallax (parallax indicates a displacement in the apparent position of an object viewed along two different lines of sight, and is measured by the angle of inclination between those two lines), we found that the quality of

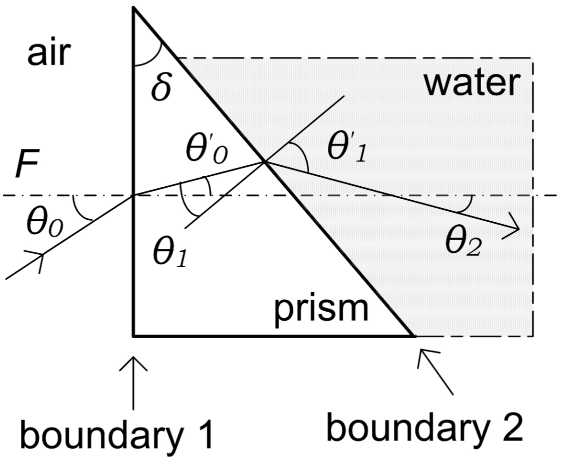

FIGURE 3.5: Design of the prism.

point detection improved when the angle of deviation of the laser beam with respect to the optical axis was 14°. To achieve the desired angle of deviation, we used an acrylic prism instead of setting a tilt angle for the optical fiber. This enabled us to scale down the diameter of the endoscope significantly.

The design of the prism is shown in Fig. 3.5. The laser beam passes through the air into the prism with an angle of incidence θ_0, and then passes through the prism yielding a refracted ray in water. The axis *F* is a reference axis parallel to the optical axis of the endoscope. The angles indicated in Fig. 3.5 can be expressed as

$$\theta_0' = \arcsin\left(\frac{n_a \sin\theta_0}{n_p}\right), \tag{3.4}$$

$$\theta_1 = \delta - \theta_0', \tag{3.5}$$

$$\theta_1' = \arcsin\left(\frac{n_p \sin\theta_1}{n_w}\right), \tag{3.6}$$

$$\theta_2 = \theta_1' - \delta, \tag{3.7}$$

where n_a = 1.00, n_p varies from 1.49 to 1.53, and n_w = 1.33 are the refractive

TABLE 3.3: θ_1, τ, and δ obtained for two different refractive indices of the prism.

n_p	Minimum	Maximum
	1.49	1.53
θ_1	53.35°	58.20°
τ	60.60°	63.46°
δ	53.35°	58.20°

indices of air, the prism, and water, respectively. Hence, the total angle of deviation of the laser beam, γ is

$$\gamma = \theta_0 + \theta_2. \tag{3.8}$$

In our case, the incident laser beam was designed to be perpendicular to the prism surface. As a result, $\sin\theta_0 = 0$ and $\theta_0' = 0$. By substituting Eqs. (3.5) - (3.7) in Eq. (3.8), the apex angle of the prism, δ, can be obtained by solving the equation

$$\frac{\gamma\pi}{180} = \arcsin\left(\frac{n_p \sin\delta}{n_w}\right) - \delta. \tag{3.9}$$

where $\gamma = 14°$ is an empirical value obtained from our previous experiments.

When a light wave strikes the boundary between two materials with different refractive indices, total internal reflection occurs when the angle of incidence is greater than the critical angle. In Fig. 3.5, the total internal reflection does not occur at boundary 1 because the angle of incidence (θ_0) is zero. For boundary 2, the critical angle between the prism and water is given by

$$\tau = \arcsin\left(\frac{n_w}{n_p}\right). \tag{3.10}$$

Table 3.3 summarizes the values of θ_1, τ, and δ for two different refractive indices of the prism. It can be seen that the apex angles of the prism obtained from Eq. (3.9) are smaller than the corresponding critical angles ($\delta < \tau$).

Several types of prism have been made with different apex angles, as depicted in Fig. 3.6(a). The one on the rightmost side was the final version with

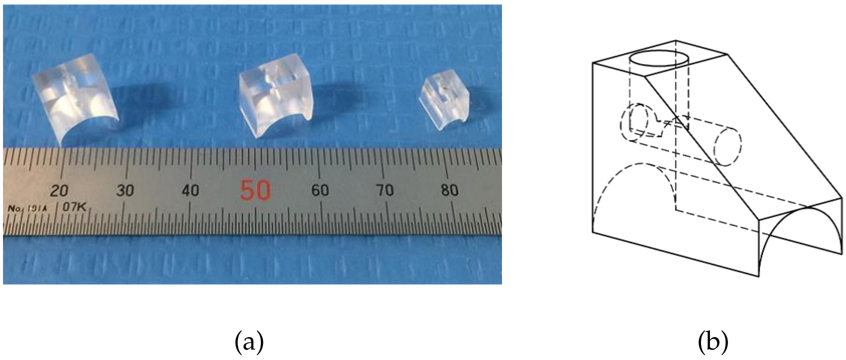

(a) (b)

FIGURE 3.6: Samples of prism: (a) prisms designed with different apex angles, and (b) structure of the prism.

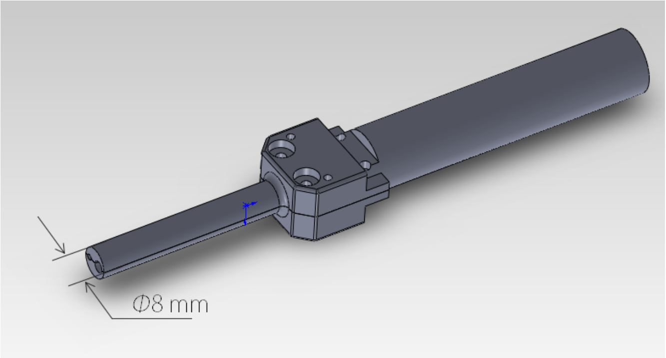

FIGURE 3.7: 3D design of the endoscopic tube.

an apex angle of 54°, which was chosen from an average value of the apex angle. Fig. 3.6(b) shows the inner structure of the prism.

3.5.2 Endoscopic Tube

A custom-manufactured endoscopic tube was designed using the SolidWorks (Dassault Systèmes, SolidWorks Corp., France), as depicted in Fig. 3.7. Camera and prism will be affixed at the tip. The diameter of the tube is approximately 8 mm.

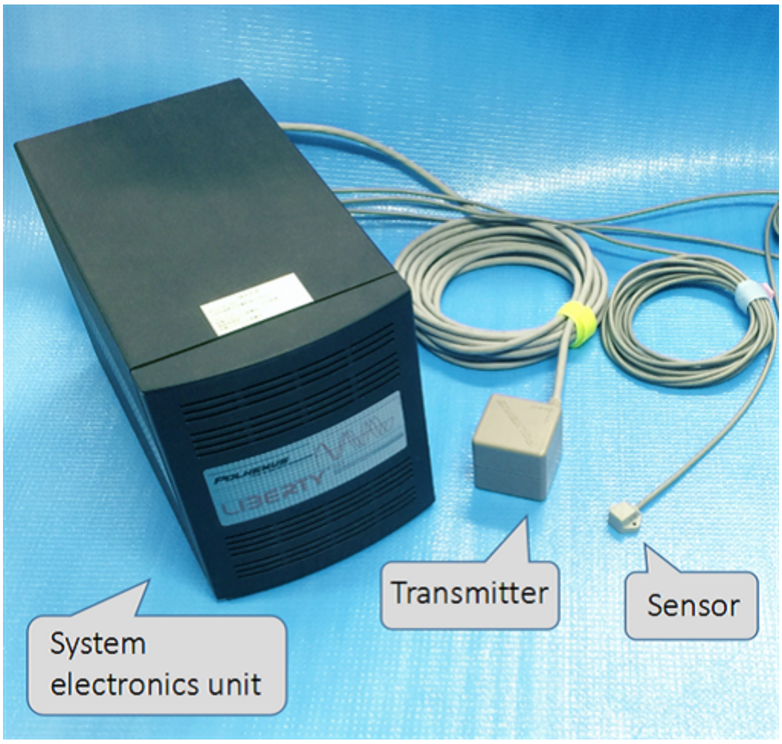

FIGURE 3.8: Electromagnetic tracking devices: LIBERTY.

3.6 Electromagnetic Tracking Device

Electromagnetic tracking devices have been widely used in spatial digitization and as a kinematic measuring tool [43]. In our experiment, a six degrees of freedom (DoF) electromagnetic device (LIBERTY, Polhemus, USA) is utilized, see Fig. 3.8. This tracking system supports four sensors and is scalable to support up to eight sensors, each operating at up to 240 Hz.

According to the manufacturer's technical literature, which suggests system accuracies of 2.5 mm root mean square (RMS) and 0.5° RMS for position and orientation respectively. Whereas, a report pointed out that this device was sensitive enough to detect positional and rotational changes of 0.25 mm and 0.1° when utilized within its optimal operating range of 225-640 mm [43].

With the aid of this device, 3D coordinates of the laser points extracted by the camera will be measured and transformed into the coordinate system of this device.

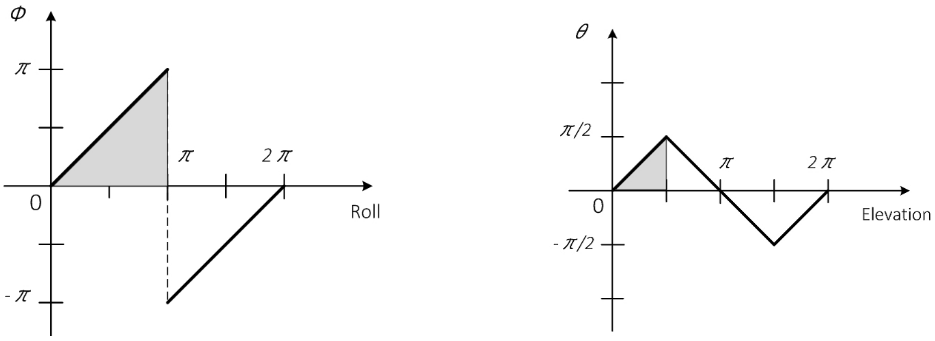

(a) The output data in roll.

(b) The output data in elevation.

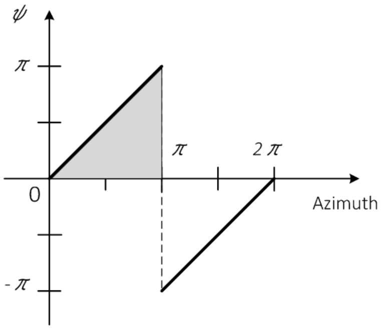

(c) The output data in azimuth.

FIGURE 3.9: Effective measurement range of the sensor's Eulerian angles.

An experiment that investigates the measurement range of the sensor was performed using the manufacture's graphical user interface. This experiment focus on the investigation of the sensor's rotation on three axes (X, Y, and Z), which refer to three Eulerian angles (roll, pitch, and yaw).

Twisting the sensor, from 0 degrees to 360 degrees, in azimuth, elevation, and roll respectively without moving its position, data of the sensor's orientation were then collected. As illustrated in Fig. 3.9, rotation in azimuth and roll were discontinuous with a measurement range of 180 degrees, the shaded area shown in Fig. 3.9(a) and Fig. 3.9(c). Although the output data in elevation were continuous, the effective measurement range was only 90 degrees, Fig. 3.9(b).

3.7 Programming

The program was edited with C++ language and compiled in the development environment of the Microsoft Visual Studio on a desktop PC with a Core i7-3770 3.4 GHz CPU and 8-GByte of RAM. In addition, due to the use of OpenCV (open source computer vision) and OpenGL (open graphics library)on the image processing and surface rendering, real-time performance of the system can be achieved.

3.7.1 Graphical User Interface

The graphical user interface (GUI) of the program was developed using C++ Builder 4.0 (Borland Co. Ltd.). The main window of the scanning control is of two functions of data exchange and precision evaluation as shown in Fig. 3.10(a). Extraction of the line laser was conducted using a separate software and the computed results were imported into the display window via shared memory technique. In order to observe the object conveniently, viewpoint assistant window was developed, which makes it extremely convenient for the user to select an optimal view angle, Fig. 3.10(b). A window for displaying the obtained surface are shown in Fig. 3.10(c). Finally, the proposed marching cubes algorithm, as well as the surface rendering, are performed by clicking buttons located in this form.

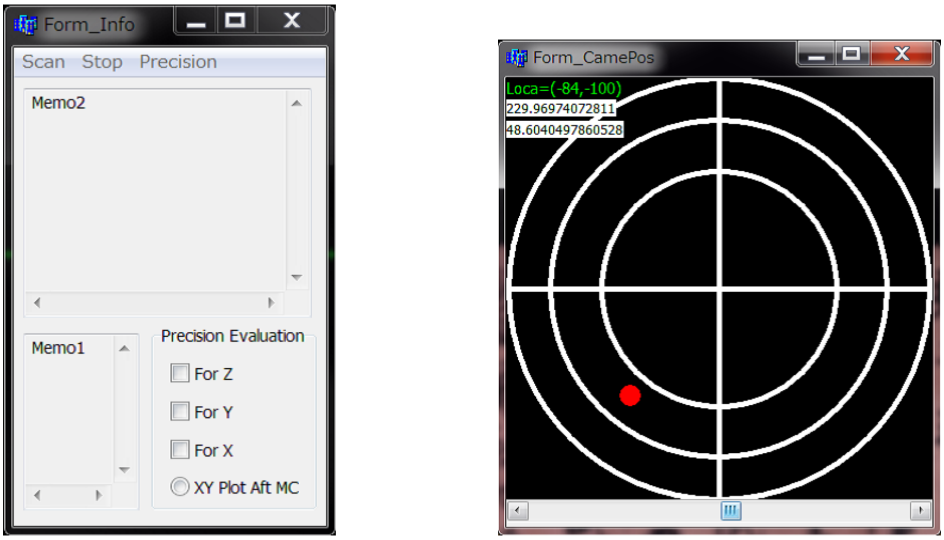

Loca=(-84,-100)
229.96974072811
48.6040497860528

(a) The form for scanning control.

(b) The form for viewpoint selection.

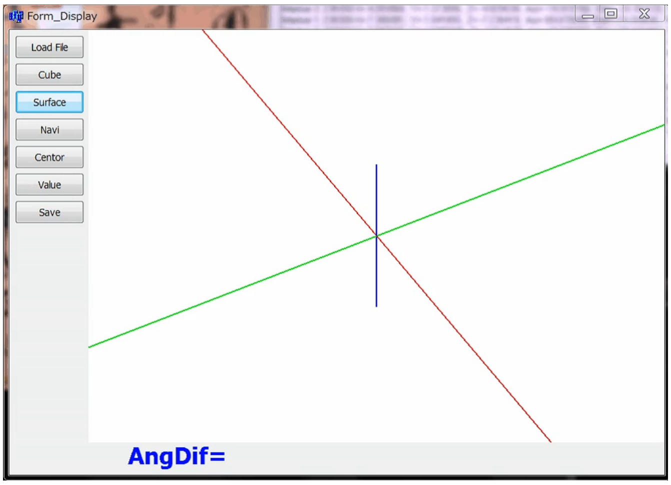

(c) The form for surface displaying.

FIGURE 3.10: Main GUI for displaying the reconstructed surface.

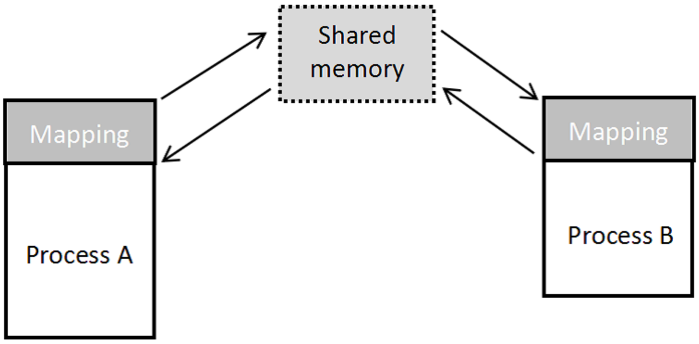

FIGURE 3.11: Process of the shared memory technique.

3.7.2 Shared Memory

Windows provide a number of application program interface (API) functions for the inter-process communication (IPC). Some functions provide for communication on the same host, while others facilitate host-to-host exchanges. In our program, one application collects and generate data, while another application progress and analyzes the information simultaneously. Hence, sharing information by reading and writing from a common segment of memory is needed to reduce the computational cost.

As its name implies, shared memory makes a common segment of memory accessible to more than one process. Notice that shared memory is not drawn from a process's own memory. Instead, the common memory is allocated from the computer system's free memory and is annexed by each process that wants access.

Fig. 3.11 depicts the process of shared memory. Firstly, two processes, A and B, are executing different code on the same host. Secondly, process A requests a segment of memory and names it so that another process can find it. Thirdly, both processed mapping the shared memory segment into their address space. Finally, the two processes can share data, including reading and writing, via the common memory.

Chapter 4

3D Visualization of the Knee Joint Surface

4.1 Introduction

Minimally invasive surgery (MIS) is an advanced technique that uses an endoscope for direct viewing of patients' internal organs for diagnosis and treatment. The use of this technique has increased considerably in the past three decades [44], [45]. MIS has advantages over traditional open surgery in terms of less trauma, lower morbidity risk, and faster recoveries. Arthroscopic surgery is a minimally invasive surgical procedure carried out on joints, most commonly used for the knee, elbow, and ankle joints. It involves examination and treatment using an endoscope. For knee arthroscopy, only two small incisions are required for the insertion of the endoscope and surgical instruments. Surgeons can view the operating field directly on a video monitor. However, in contrast to open surgery, MIS cannot provide surgeons with stereo visual perception of the surgical target. Surgeons have to rely upon motion parallax, object exclusion, and other indirect evidence of depth to assess the spatial relationship of objects in the operating field [46].

In order to enhance the surgeon's depth perception during MIS, image-guided systems [47], [48], robotically assisted approaches [49], [50], and various optical techniques including passive and active methods [51] have been developed in the recent past. These methods focus mainly on three-dimensional (3D) surface reconstruction of surgical targets. For example, the first study on stereoscopic depth reconstruction in MIS using parallel implementation of stereoscopic matching algorithms was reported in [52], and corresponding experiments were performed to construct the 3D model of an organ using a robotized stereoscopic endoscope [53]. A new image modality for 3D visualization of human organs, proposed in ref. [54] uses laparoscopic image sequences, and is based on feature tracking. However, such an approach cannot be used in real time because it involves selecting a set of image subsequence for surface recovery. Furthermore, this approach requires iterations of a factorization method that would increase the computational time. In contrast, a novel technique operating in real time that uses motion tracking based on feature matching has been reported to perform well for the surface recovery of a phantom model and various *in vivo* endoscopic images [55]. However, it should be noted that all the above-mentioned techniques are used for surface recovery of soft tissue or human organs rather than in arthroscopic surgery, especially for the knee joint. The reason for this is that the optical properties of the knee joint imaged by different cameras vary from case-to-case.

While stereo vision is used for feature matching, structured-light techniques are used for detecting the projected patterns correctly. Compared to stereoscopic techniques, structured-light techniques are faster and more accurate. An early study [56] used an endoscope with structured light for measuring the profile of a gastrointestinal surface. Although this method was able to restrict the measurement error to an average value of 0.05 mm, it provided surgeons with only an approximate estimate of the absolute distance to the surface of the object. Thus, depth perception of the surgical target remained difficult. Moreover, the instrument size was considerably large, the total diameter of the endoscope and fiber bundle being as large as 20 mm. Subsequently, a similar system [57] using an endoscope and image fiber was reported for high-speed measurement of a lesion area. However, in this system, the required distance between the endoscope tip and surface of the object during scanning was 50-70 mm. Such a large distance makes it unfeasible for application in arthroscopy. Furthermore, the large size of the endoscope tip (16 mm diameter) was the main limitation of this particular system. Nevertheless, systems using structured light and miniaturized optical components are being employed increasingly in MIS. For instance, a flexible probe with a diameter of 1.7 mm has been developed recently [58]. It uses a multispectral pattern projected using a supercontinuum laser. The projected points with a specific wavelength are recorded by a color endoscope camera, and can be segmented depending on their color values and spatial coordinates. The most attractive features of this report are that the probe itself is sufficiently small to be used in combination with a flexible medical endoscope, and the study has been performed on *ex vivo* tissue surface in real time. However, the authors have not specified the size of the endoscope in their report. Moreover, as in the case of stereo vision-based systems, techniques using structured light also focus on the surface recovery of human organs and/or soft tissues in MIS. To the best of our knowledge, there have been no reports on the 3D surface reconstruction of knee joints in arthroscopic surgery till date.

In this chapter, we propose a fiber-based endoscopic system for reconstructing the surface of the knee joint during MIS. Our experiments have revealed that the proposed system can recover a 3D surface from a moving endoscope. More importantly, our system can perform in a narrow operating field. We have used a green line laser for creating the illumination pattern. An optical fiber is used to project the line laser on the surface of the object. Additionally, a prism is used to decrease the length and diameter of the baseline and endoscope tube, respectively. Surface reconstruction is achieved by calculating the spatial location of the laser spots using the optical triangulation method.

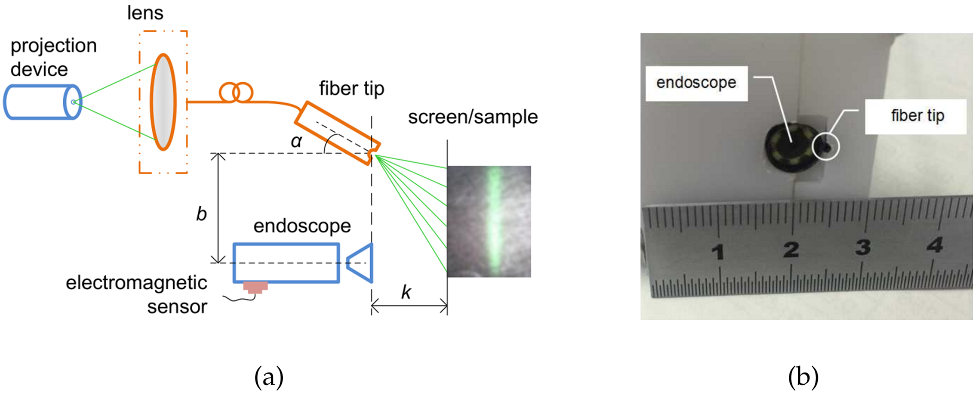

(a) (b)

FIGURE 4.1: Endoscopic system I: (a) configuration of endoscopic system I, and (b) endoscope tip.

4.2 Methodology

In this section, we describe two endoscopic systems. The first system (system I) is a previous system that tests in the air, while system II is developed to test underwater. Although there are some differences in the system setup, the calculations of data are the same methodology.

4.2.1 Configuration of Endoscopic System I

The endoscope system I is mainly composed of an endoscope and a fiber, as depicted in Fig. 4.1(a). A lens, one end of the optical fiber, was connected to the projection device of a line laser. The line laser was projected onto the object surface by the fiber tip, which is the other end of the fiber. Distance b indicates the baseline, and distance k indicates the scanning gap.

Additionally, the endoscope was fixed to the fiber tip with a small tilt angle α (angle between fiber center and the optical axis of the camera). In this situation, it is easier and more sensitive to extract the line laser from the image sequences due to the existence of parallax. The optical fiber and endoscope are fixed using a custom-manufactured holder, as shown in Fig. 4.1(b).

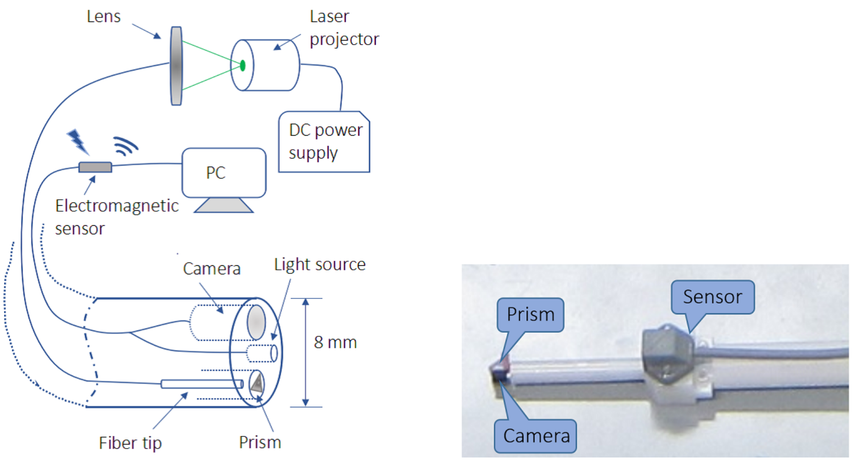

(a)

(b)

FIGURE 4.2: Endoscopic system II: (a) configuration of endoscopic system II, and (b) endoscope tip.

4.2.2 Configuration of Endoscopic System II

The configuration of endoscopic system II is illustrated in Fig. 4.2(a). A lens with optical fiber (Asahi Kasei Corp., Japan) on one side is attached to a laser beam irradiation device. On the other side, a fiber tip with a diameter of 1 mm is inserted into a prism designed using a certain angle applied in underwater experiments. With this configuration, the brightness of the laser beam can be transmitted sufficiently to the knee joint surface. Furthermore, the customized acryl prism results in a relatively long baseline while allowing the endoscope tube to remain small. The distance between the camera and the optical fiber is the baseline length, and is 6 mm in the current system.

In addition, a 3.9-mm diameter camera (I-O Data Inc., Japan) with a video resolution of 360 pixels × 240 pixels is fixed to the prism in an axially aligned configuration. As a consequence, the diameter of the endoscope tube is approximately 8 mm, which is a significant improvement over our previous system [59], which was limited to applications outside the body. Moreover, the size of the endoscope tube (8 mm) matches the diameter of the graft-harvesting tool [30]. The endoscope tip of system II fixed with the holder II is shown in Fig.

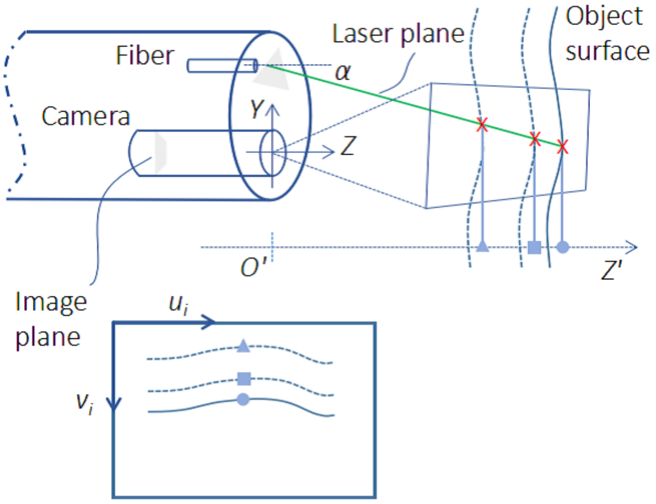

FIGURE 4.3: Object projection on the camera system.

4.2(b). To further enhance the current system, we employed a DC power supply for the laser projector, which adjusts the input voltage of the projector based on different environments, e.g., the level of brightness or material used.

4.2.3 2D Data Acquisition

A schematic of the object projection in the camera system is illustrated in Fig. 4.3. A laser passing through the prism illuminates a line laser on the object surface, which is observed by the camera. Axis Z' is a reference axis parallel to the depth axis (Z) of the endoscopic camera, and α is the deviation angle of the laser with respect to the Z axis. Depth changes of the object surface are reflected in the v_i axis located on the image plane. Laser points are then segmented in a frame-by-frame manner depending on their color values and weighted average of intensity [56].

For frame n-1, given a series of points S_i of the surface and its corresponding locations s_i^{n-1}=$[u_i, v_i]^T$ on the image plane (i is the index of the u_i axis), a trigonometric relationship is yielded. The coordinates in the camera system, $S_{i,c}^{n-1}$, can be express as

$$S_{i,x}^{n-1} = \frac{S_{i,z}^{n-1}(u_i - u_o)}{f}, \tag{4.1}$$

$$S_{i,y}^{n-1} = \frac{S_{i,z}^{n-1}(v_o - v_i)}{f}, \tag{4.2}$$

$$S_{i,z}^{n-1} = \frac{bf}{(v_o - v_i) + f \cdot \tan\alpha}, \tag{4.3}$$

where f is the focal length of the camera, (u_o, v_o) are the coordinates of the principle point, and l is the baseline length.

The coordinates in the camera system, Eqs. (4.1-4.3), could be represented as followings

$$S_{i,\mathbf{c}}^{n-1} = [S_{i,x}^{n-1}, S_{i,y}^{n-1}, S_{i,z}^{n-1}]^T \tag{4.4}$$

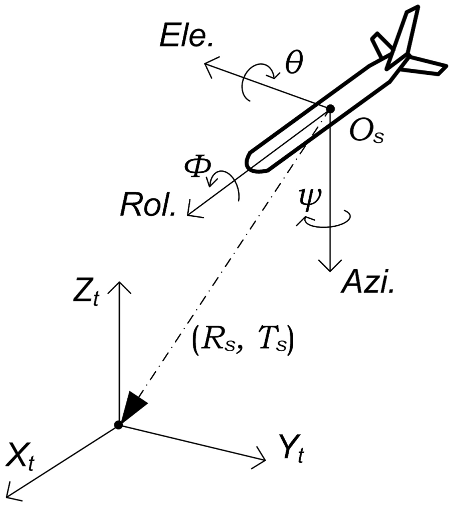

FIGURE 4.4: Euler angles of the sensor. O_s denotes the sensor's electrical center. X_t, Y_t, and Z_t denote the three axes defining the coordinate system of the transmitter.

4.2.4 3D Reconstruction

The position of the line laser was calculated and recorded by measuring its six degrees of freedom (DoF) using a state-of-the-art electromagnetic device (LIBERTY, Polhemus Inc., USA) consisting of one transmitter and three sensors. Two of the sensors are fixed to the endoscope (sensor 1) and the scanning object (sensor 2) respectively, and the other one is fixed to the harvester (sensor 3) for navigation. The transmitter is a magnetic source and produces an electromagnetic field, which is an accurate reference of the 6DoF position and orientation measured by the sensors. The coordinate system of the transmitter was defined to be the coordinate system of the real world.

The Euler angles of the sensor, namely, the azimuth, elevation, and roll are represented by ψ, θ, and ϕ in Fig. 4.4. These angles represent an azimuth-primary sequence of frame rotations that define the sensor's current orientation corresponding to the zero-orientation state ($\psi = 0$, $\theta = 0$, $\phi = 0$) of the transmitter. The rotation sequence can be defined as

$$\tilde{\boldsymbol{R}}_s = \boldsymbol{R}(\psi)\boldsymbol{R}(\theta)\boldsymbol{R}(\phi), \tag{4.5}$$

where

$$\boldsymbol{R}(\psi) = \begin{bmatrix} \cos\psi & -\sin\psi & 0 \\ \sin\psi & \cos\psi & 0 \\ 0 & 0 & 1 \end{bmatrix}, \tag{4.6}$$

$$\boldsymbol{R}(\theta) = \begin{bmatrix} \cos\theta & 0 & \sin\theta \\ 0 & 1 & 0 \\ -\sin\theta & 0 & \cos\theta \end{bmatrix}, \tag{4.7}$$

$$\boldsymbol{R}(\phi) = \begin{bmatrix} 1 & 0 & 0 \\ 0 & \cos\phi & -\sin\phi \\ 0 & \sin\phi & \cos\phi \end{bmatrix}. \tag{4.8}$$

Consequently, the coordinate transformation from the camera system into 3D world coordinates is given by

$$S_{i,\mathbf{w}}^{n-1} = \tilde{\boldsymbol{R}}_s[S_{i,\mathbf{c}}^{n-1} + \boldsymbol{L}_r] + \boldsymbol{T}_s, \tag{4.9}$$

where $\tilde{\boldsymbol{R}}_s$ is a square 3×3 matrix defining the rotation sequence of the sensors, $\boldsymbol{L}_r$ represents the relative distance between the camera and sensor 1, and $\boldsymbol{T}_s$ is a translation vector with respect to the transmitter coordinate system.

Eventually, the extracted point set $\mathbb{R}^3$ from the frame of an image sequence (frame 1 to frame n) is given by

$$\mathbb{R}^3 = \sum_{k=1}^{n} S_{i,\mathbf{w}}^{k}, \tag{4.10}$$

where n is the total number of frames, and Σ indicates the union of spatial points.

4.3 Vertex Configuration

In general, the classical marching cubes (CMC) algorithm processes the 3D medical images obtained from computed tomography (CT) or magnetic resonance imaging (MRI), while the volumetric data described in this work are based on endoscopic images. Before displaying the reconstructed surface, a process named vertex configuration is required. Thus, in this section, a modified marching cubes algorithm is presented for the point set $\mathbb{R}^3$ of the reconstructed surface.

4.3.1 Classical Marching Cubes Algorithm

The use of CMC algorithm, as originally described by W. Lorensen and H. Cline [60], is probably the most popular approach for extracting isosurfaces from a volumetric dataset [61]. Since the CMC technique makes it easier for surgeon to observe and visualize an object in a better sense, it has been applied to many medical applications to overcome the difficulty of imagination related to the complicated anatomical structures of organs or soft tissues. For example, authors [62] proposed a novel and efficient implementation of the MC to reconstruct anatomical structures. An improved MC algorithm reported in [63] was used for modeling the pleural surface of the chest wall.

Commonly, past usage of many volumetric datasets often involved the 2D cross-sectional "slices" that derived from a CT or MRI. One sample of CT slice is shown in Fig. 4.5. These datasets can be segmented and viewed as a stack of intersections with numbers of parallel planes, corresponding to a sequence of 3D image slices [62]. For each slice, the CMC takes it as a regular 3D grid and each intersection of such a grid is called a voxel. A voxel (volumetric pixel) is a volume element, and a scalar value (voxel content) is associated with it [64].

As illustrated in Fig. 4.6, one logical cube defined by eight neighboring voxels within adjacent slice S_k and S_{k+1} ($1 < k < n$, where n is the number of slices). Thus, the voxels lay on row x_i ($\forall\ i$) and column y_i ($\forall\ i$) of the slice S_k is

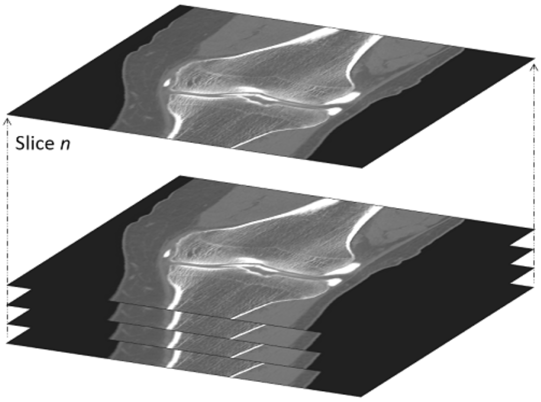

FIGURE 4.5: Volumetric dataset of a knee joint.

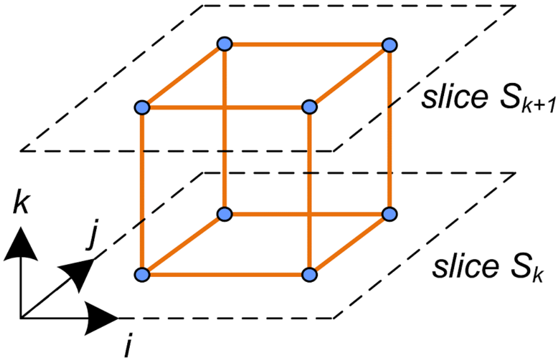

FIGURE 4.6: Formation of a logical cube.

directly adjacent to the next voxels, which lay on row x_i and column y_i of the slice S_{k-1} and S_{k+1}.

Using a divide-and-conquer approach, the CMC processes the volumetric dataset cube-by-cube to make up the volume. Given an isovalue, v_{iso}, then the related isosurface can be defined as a function $v_{iso} = v\ (x, y, z)$ that associates v_{iso} to a set of 3D points arranged on the edge of each logical cube. In terms of the isovalue, the volume dataset is divided into two groups, one with $v > v_{iso}$ inside the isosurface itself, and the other with $v < v_{iso}$ outside. Besides, in order to find the isosurface intersection in each cube, the voxels at the eight vertexes of the logical cube are compared against the v_{iso} and an eight-bit binary number corresponding to each voxel is generated.

The voxels contained in a cube inside the isosurface are associated with 1, while the voxels outside are associated with 0. Based on the eight-bit binary number, isosurface intersection algorithm is then performed within each cube.

The exact position of the triangle intersection can be calculated with sub-vertex accuracy by a linear interpolation for each intersected edge. For example, a unit-length edge E^1 has end points P_s and P_e, whose scalar values are v_s and v_e, respectively, the 3D position of intersection I is then given by the following equation [65]

$$I_{(x,y,z)} = P_{s(x,y,z)} + \Delta t\Big(P_{e(x,y,z)} - P_{s(x,y,z)}\Big), \tag{4.11}$$

where

$$\Delta t = \frac{v_{iso} - v_s}{v_e - v_s}. \tag{4.12}$$

The last step in CMC is to estimate the gradient vector using finite difference method for each triangle vertex, which is required for calculating the surface normal. Besides, dividing the gradient vector by its length yields the unit normal of the vertex required for the rendering algorithm. At this step, four slices have to be loaded into the memory at one time.

4.3.2 Proposed Marching Cubes Algorithm

Because the volumetric data obtained by our system are not as uniformly spaced as those obtained from CT or MRI, the traditional marching cubes algorithm cannot be applied directly in this work. Hence, the process of vertex configuration was performed based on our proposed marching cubes (PMC) algorithm [59]. This process makes use of an improved marching cubes algorithm that arranges the volumetric data using midpoint comparison to construct 3D regular grids.

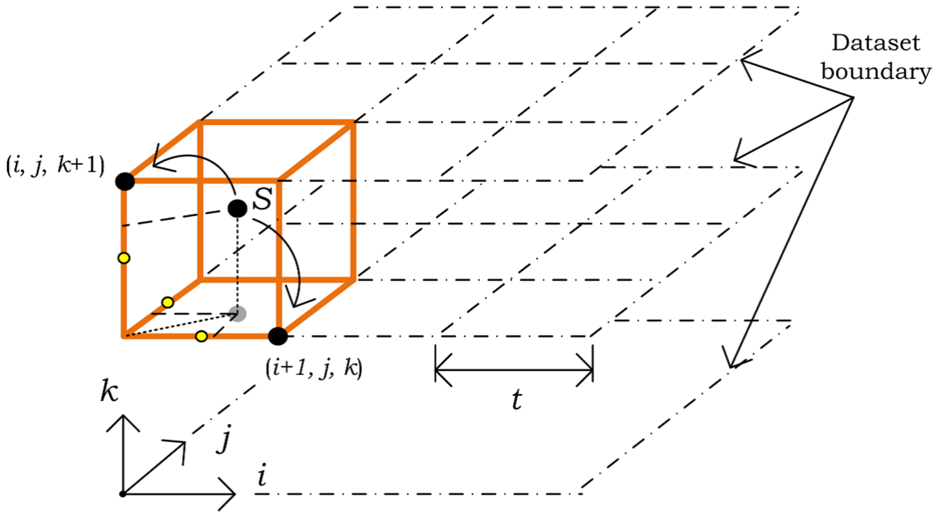

FIGURE 4.7: Example of vertex configuration. The yellow points denote the midpoints of each axis. t is the cubic interval.

To summarize, the PMC algorithm consists of three parts as followings:

- 3D Grid Arrangement
- Surface Extraction
- Surface Rendering

(1) 3D Grid Arrangement

The process of vertex configuration is demonstrated in Fig. 4.7. First, we project a physical point S among the volumetric data on the three perpendicular axes. If the projection distance along a certain axis exceeds the corresponding midpoint, which is defined by the length of the edge of the cube, a binary number 1 is assigned to the vertex, for example, $(i, j, k+1)$, and $(i+1, j, k)$. On the other hand, if the projection distance along a certain axis is less than the corresponding midpoint, a binary number 0 is assigned to the vertex.

Cubic interval, t, determining the size of the cube is set in advance. As we observe in various results, parameter setting of t affects the overall effect of the reconstructed surface. Fig. 4.8 illustrates several cubic interval settings [66]. In the case of t = 2.54 mm and t = 5.08 mm, shapes of the surface could not be adequately reconstructed and some detailed information were lost, since the interval setting was over big, Fig. 4.8(a) and Fig. 4.8(b). However, we can see a lot of 'holes' on the rendered surface in the case that t = 0.635 mm. These holes may be due to the fail of the surface extraction process. Finally, interval t being 1.27 mm could obtain a smooth surface, Fig. 4.8(c). A 3D grid was then yielded using the PMC algorithm, see Fig. 4.8(e). Fig. 4.8(f) shows the femoral bone surface tested in this experiment.

Under this assumption, a regular 3D grid is then generated after finishing a loop among the volumetric dataset. Note that the original volumetric dataset is then replaced by this regular 3D grid, which is used for the next step: surface extraction.

(2) Surface Extraction

The proposed algorithm employs the CMC look-up table to produce the surface intersection. Taking account of the reflective and rotational symmetries of a cube, the authors, Lorensen and Cline [60] reduced all possible combination from 256 cases ($2^8 = 256$) to 15 basic patterns, see Fig. 4.9, some works have described only 14 basic patterns [67]–[69].

The simplest pattern, 0, implies that there is no spatial point within the cube at all and thus produces no triangles. The next pattern, 1, implies that only one vertex contained in the cube receives a binary one.

A method proposed by C. Montani *et al.* [70] is utilized to obtain the exacted position of the surface intersection. In contrast with the CMC, this method based on midpoint selection does not require any interpolation along with the edge of cubes in surface extraction processing. When a cube edge with a binary number, zero or one, the midpoint of the edge is the intersection being looking for.

The midpoints in a cube that can be yielded via midpoint selection are shown in Fig. 4.10: there are 12 different spatial positions (the white circles from #1 to #12) on which triangle vertexes can be intersected. Moreover, an index consists of eight-bit binary number is created based on the state of the vertex to record its position. Using the vertex index shown in Fig. 4.10 (the black circles from #1 to #8), the eight-bit index contains one bit for each vertex.

This index serves as a pointer into an edge table that gives all edge intersections for a given surface extraction [60].

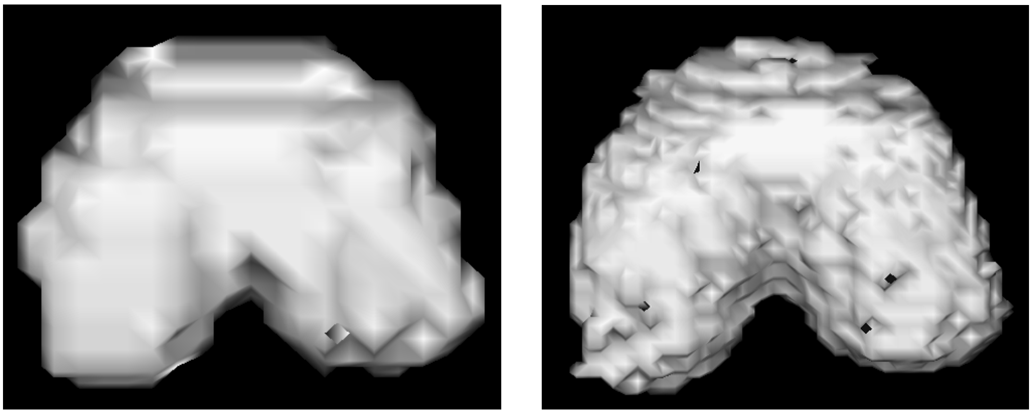

(a) $t = 5.08$ mm (b) $t = 2.54$ mm

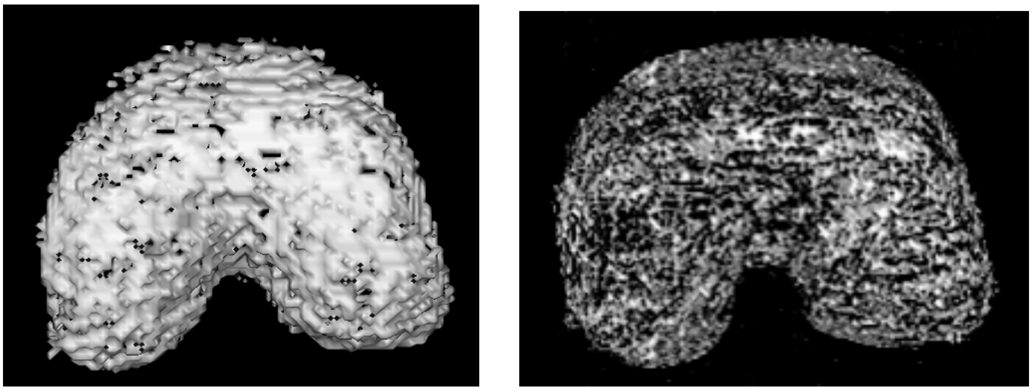

(c) $t = 1.27$ mm (d) $t = 0.635$ mm

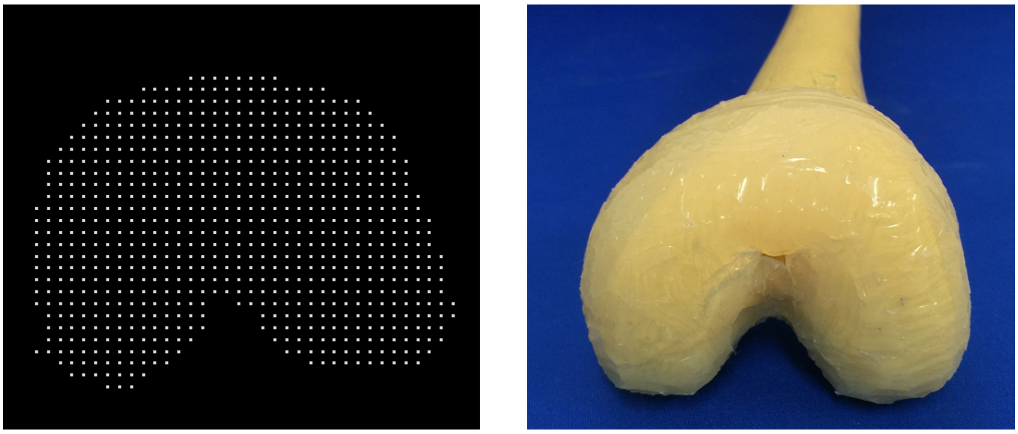

(e) The 3D grid result corresponding to (c) (f) The tested bone surface

FIGURE 4.8: Cubic interval (t) setting and its result.

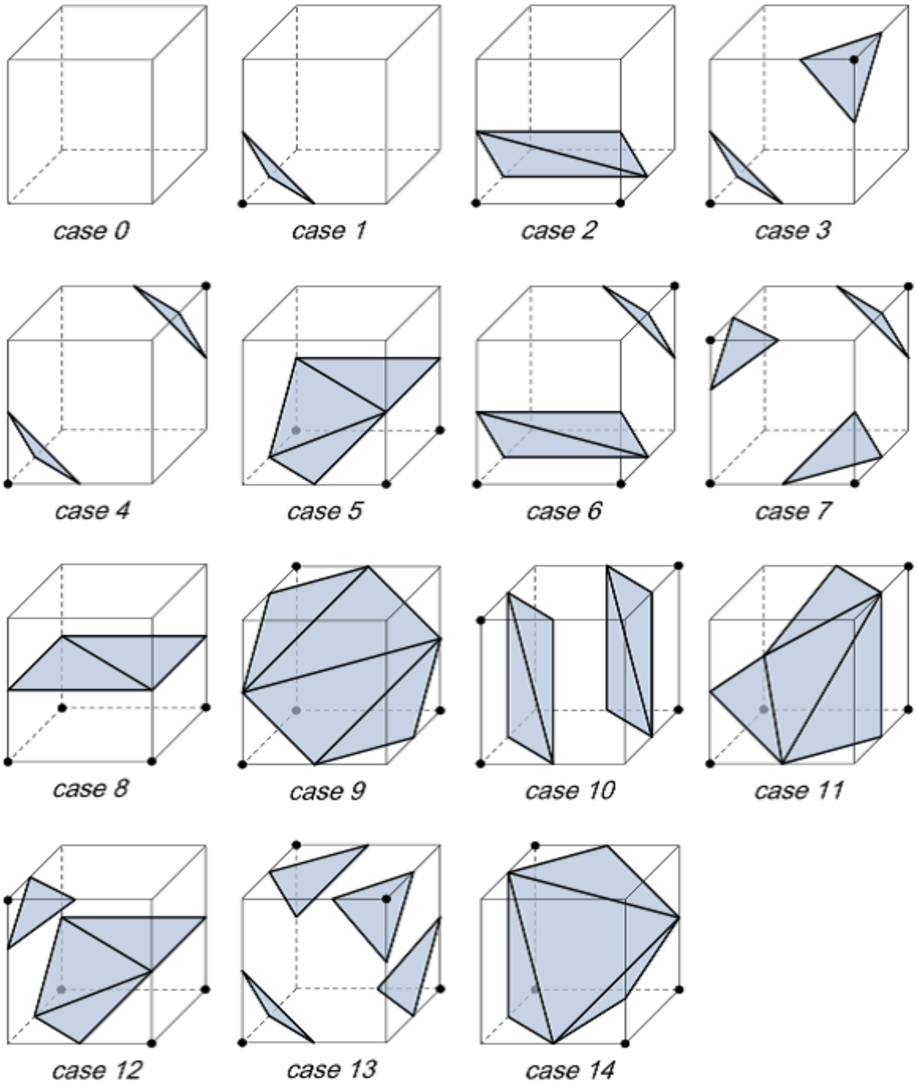

FIGURE 4.9: Type of surface combinations for the CMC algorithm. The black circles mean that vertexes inside the surface.

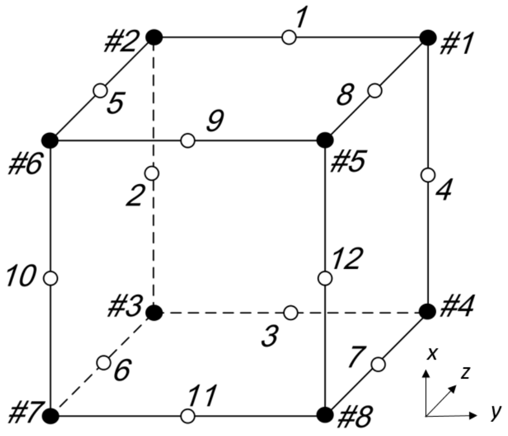

Index =	#8	#7	#6	#5	#4	#3	#2	#1

FIGURE 4.10: Index for vertex position.

(3) Surface Rendering

Volumetric dataset are often rendered with indirect volume rendering (IVR) technique [71]–[74] , such as the CMC algorithm, which involves the rendering of an intermediate structure (e.g., an isosurface) that has been extracted from the dataset, typically via automatic means [65]. In contrast, the render method used in our system is the OpenGL technique due to the dataset type differs from those of CMC. In order to reduce the overall computational time, the positions of triangle vertexes intersected on the cube edge (256 cases) are computed in advance depending on the look-up table. The detailed calculation is saved in a list included in the rendering program.

The final step in the PMC calculates a unit normal for each triangle vertex, which is used for surface rendering. Since the direction of the gradient vector, ∇g, is normal to the surface, we can use this fact to determine the surface normal vector if the magnitude of ∇g is nonzero [60].

The calculation of gradient vector reported in the CMC were base upon the central differences. As mentioned above, however, the volumetric data obtained by our system are different, because we could not get the density of each pixel as like the CT/MRI slice.

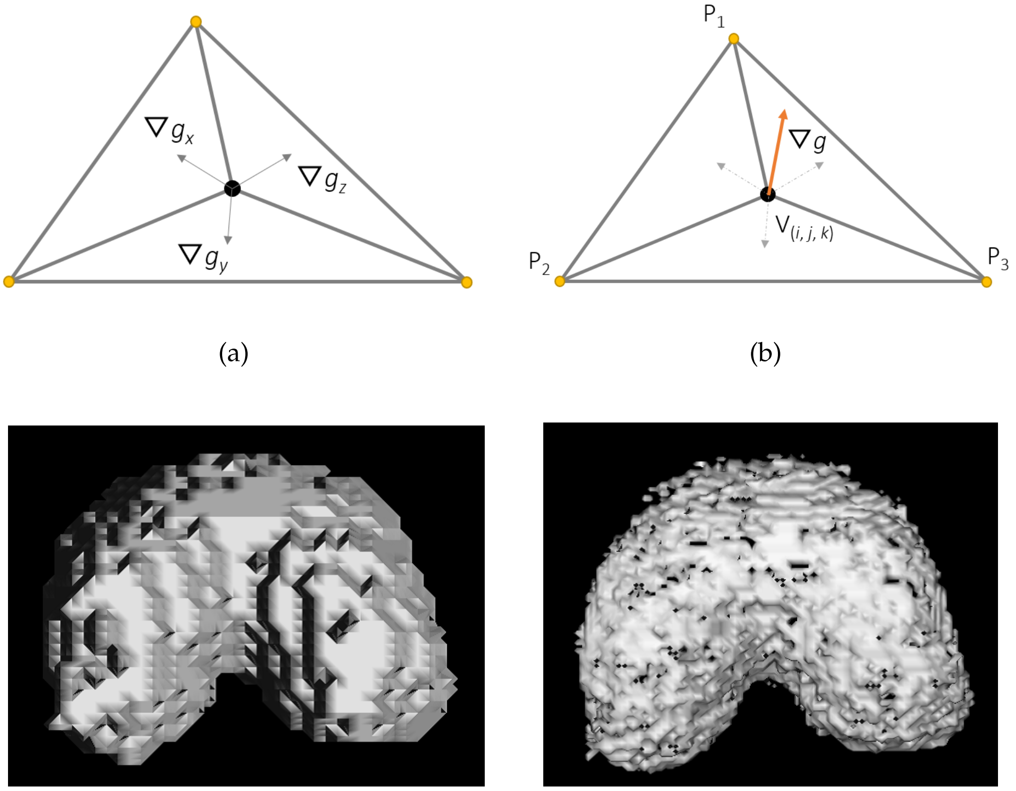

(a) (b)

(c) (d)

FIGURE 4.11: Gradient calculation of the cube vertex: (a) the gradient at cube vertex, (b) calculated unit normal, (c) surface rendering without unit normal, and (d) surface rendering with unit normal.

In our case, the gradient at a cube vertex is concerned with three directions. As illustrated in Fig. 4.11(a)-4.11(b), the black point, V, is the cubic vertex, and the smaller points, P_1, P_2, and P_3, mean that vertexes inside the triangulated surface. Hence, the gradient is then estimated by

$$\nabla g_x(i,j,k) = \overrightarrow{VP_1} \times \overrightarrow{VP_2}, \tag{4.13}$$

$$\nabla g_y(i,j,k) = \overrightarrow{VP_2} \times \overrightarrow{VP_3}, \tag{4.14}$$

$$\nabla g_z(i,j,k) = \overrightarrow{VP_3} \times \overrightarrow{VP_1}. \tag{4.15}$$

Dividing the gradient by its length then generate the unit normal [60], ∇g, at the vertex required for surface rendering, see Fig. 4.11(b). The rendering algorithm use this unit normal to produce triangulated surface. In addition, we can use this normal to determine the angle of illumination source. The result of surface rendering without the unit normal is shown in Fig. 4.11(c), whereas in Fig. 4.11(d) the surface is rendered with the unit normal. Obviously, the latter is much smoother and more detailed features are recovered.

In summary, the process of our proposed algorithm can be broken down into the following steps:

Step 1: Scan and acquire the dataset from the endoscope system.

Step 2: Set the interval cube parameter to create logical cubes. Normally, the default value is 1.27 mm.

Step 3: Yield the regular 3D grid by comparing the projection distance against the midpoint of cube edges.

Step 4: Obtain the type of surface extraction based on the eight-bit binary index.

Step 5: Calculate the positions of surface intersection via midpoint selection method.

Step 6: Render the triangle vertex coordinates to generate the surface.

4.4 Experimental Results of System I

The primary goal of this work is to develop a fiber-based endoscopic system for surface reconstruction. The experiments described in this chapter can be classified into two groups.

The second experiment using system II is used for the underwater test. It is no easy task to gain the 3D imaging in the water, especially in the environment of flowing water. Consequently, the previous experiment with system I were designed to demonstrate the feasibility of using this technique. Besides, we performed this experiment to show the relationship between accuracy and baseline setting. These preliminary findings were reliable for us to design the system II.

4.4.1 Reconstruction of Planar Surface

A plane of wood was placed in front of the endoscopic tip. Data collection of three distances with an interval of 5 mm was carried out. Planar reconstruction is estimated by the depth values (z coordinates of the point cloud).

Fig. 4.12(a) shows the three groups' data. The laser projection device employed in our system has a property that the best focusing performance occurs only if the scanning gap is less than 20 mm. That is why the data of the third group (20 mm) fluctuated stronger than the others. Besides, the line laser is rarely extracted from the image plane when the scanning gap <8 mm.

The average errors were found to be around 0.50 mm with the standard deviation (SD) being 0.503 mm, 0.899 mm and 1.480 mm respectively, Fig. 4.12(b). On the basis of these data, it can be concluded that scanning gap ranging from 10 to 20 mm can ensure us to obtain a better result.

Results shown in Fig. 4.13(a) is a point cloud of over hundred thousand spatial points. Using the PMC, 3D grid and surface rendering were then generated, Figs. 4.13(b)-4.13(d).

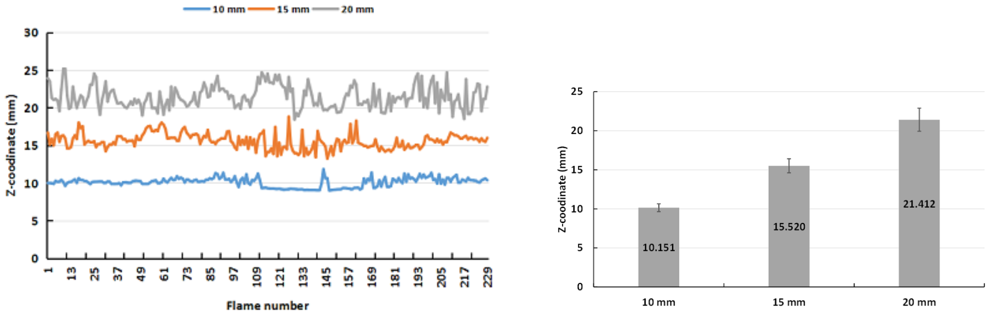

(a) (b)

FIGURE 4.12: Experimental results of a wood plane: (a) depth value evaluation, and (b) average accuracy and SD.

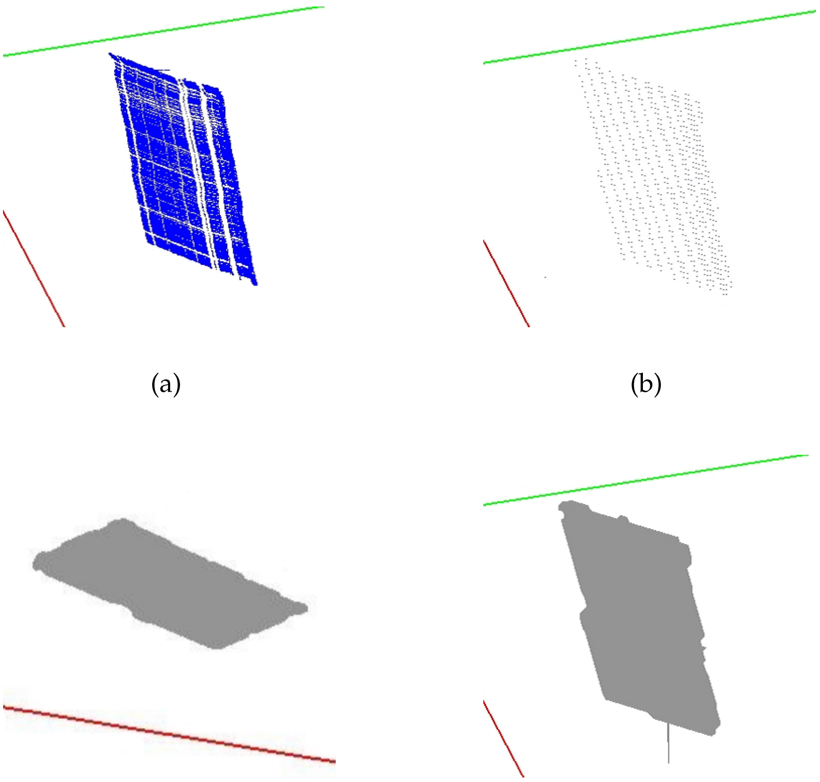

(a) (b)

(c) (d)

FIGURE 4.13: Reconstructed result of a wood plane: (a) extracted point cloud, (b) 3D grid, (c) and (d) surface rendering in different view point.

4.4.2 Reconstruction of Surface

A standard wood cylinder (49 mm in diameter) was utilized for the experiment of precision evaluation, Fig. 4.14(a). The endoscope was put close to the cylinder with a gap of 15 mm and moved along the surface by hands. A quarter of the curved surface was obtained as shown in Fig. 4.14(b). 3D grid and surface rendering are depicted in Figs. 4.14(c)-4.14(d).

To our knowledge, given a series of points (x_i, y_i), circles can be represented algebraically by an equation of the form

$$(x_i - a)^2 + (y_i - b)^2 = r^2, \tag{4.16}$$

where (*a*, *b*) is the center coordinates and *r* is the radius.

Moreover, if the points distributed in a ring-shape on the *xy*-plane approximately, we can use the least squares fitting (LSF) algorithm to find the equation of the circle that provides the best fit to the data points. The LSF implemented in Matlab (The MathWorks, INC., USA) allows us to estimate the accuracy of surface reconstruction. This method was also adopted by Neil T. Clancy *et al.* in their recent works [58].

Finally, we calculated the equation of the fitting circle as below

$$(x - 120.823)^2 + (y + 39.893)^2 = 23.322^2. \tag{4.17}$$

Extracted cylinder surface, as well as its center coordinates, are depicted in Fig. 4.14(e). The fitting diameter was 46.637 mm (SD, 0.759). These data lead us to conclude that the error of system I was 2.393 mm.

In addition, an imitation bone was chosen to test the whole effect of reconstruction. As shown in Fig. 4.15, endoscopic system I was able to recover most of the surface details.

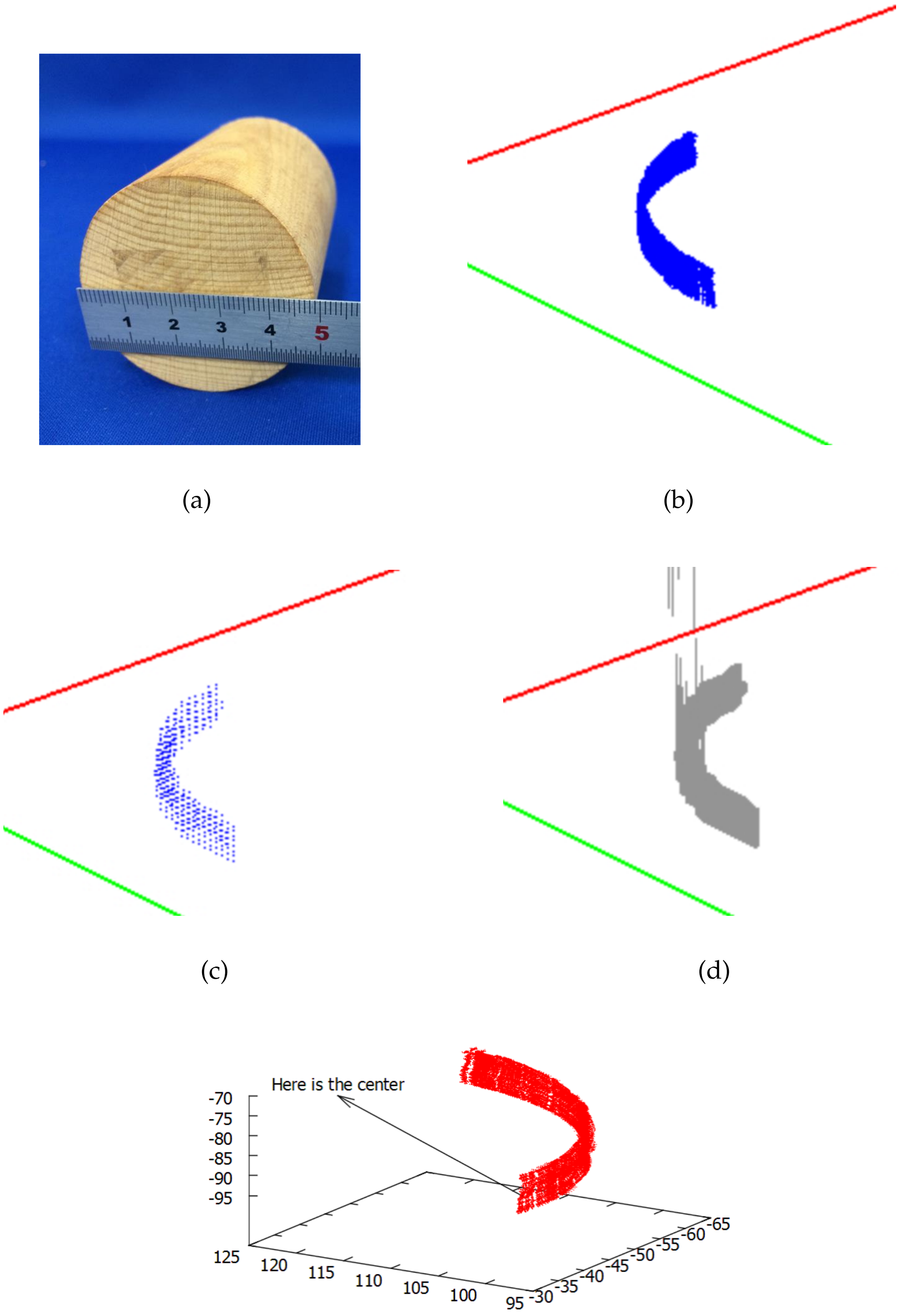

(a) (b)

(c) (d)

(e)

FIGURE 4.14: Surface reconstruction of wood cylinder: (a) cylinder model, (b) extracted point cloud, (c) 3D grid arrangement, (d) surface rendering, and (e) plot of the point cloud. The arrow denotes the center coordinates.

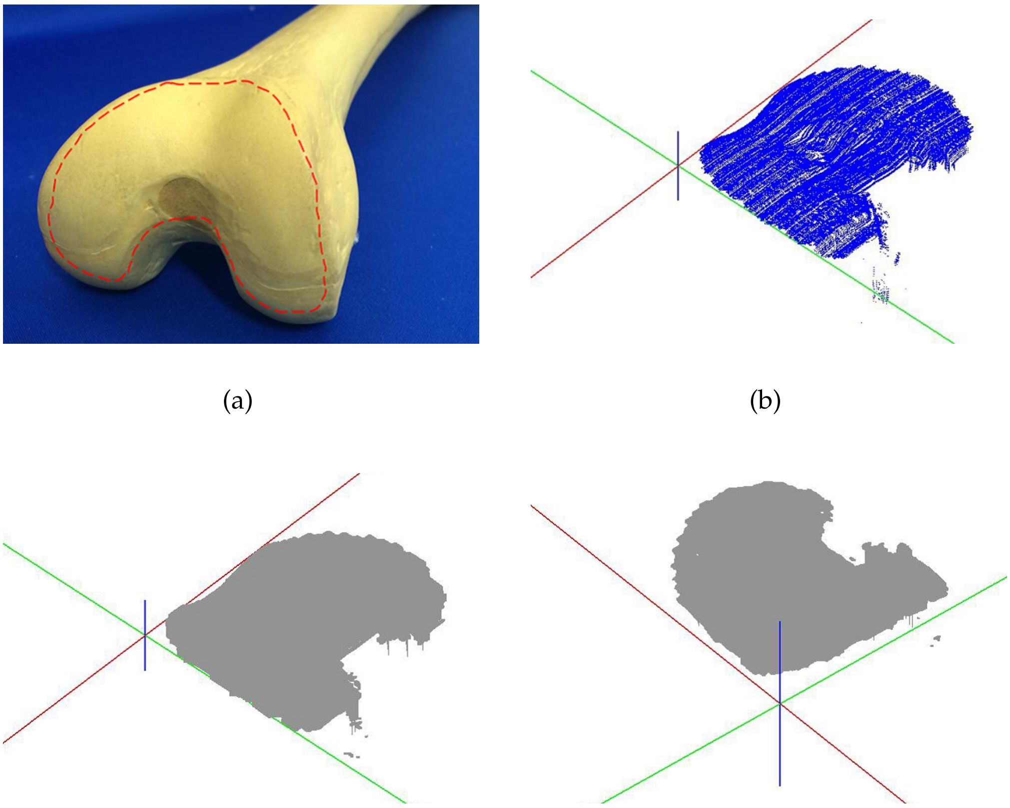
(a) (b)

(c) (d)

FIGURE 4.15: Surface reconstruction of an imitation bone: (a) figure of the bone surface, and the marked area was used for scanning, (b) extracted point cloud, (c) and (d) surface rendering in different view point.

4.4.3 Discussion

In this section, we proposed the fiber-based endoscopic system I to reconstruct 3D surfaces. This system can be achieved in real-time and the reconstructed error of plane and surface was 0.5 mm and 2.4 mm, respectively. However, the performance of this system is limited to the environment of in the air and outside the human body.

On the other hand, system I described in this section mainly seeks to demonstrated the feasibility of using an optical fiber fixed to the camera with a non-parallel way (a tilt angle of 14 ° between fiber center and the optical axis of the camera). The experimental results have shown that by using the configuration of system I it is possible to obtain 3D imaging of the objects. Based on these data and fact, we proposed a modified version (system II) that can recover a 3D surface in narrow operation field, being the endoscopic tube small in size. Experiments of using system II will be described in the following section.

4.5 Underwater Experimental Results of System II

4.5.1 Reconstruction of Planar Surface

A model of a planar surface of wood was employed to test the accuracy of the proposed system. The model was placed underwater during data collection, and the endoscope was moved manually across the surface with the different scanning gaps measured using a ruler. The range of the scanning gaps used was 10-20 mm. This range was chosen based on the actual distances from which surgeons usually make observations in real medical cases [56].

Fig. 4.16(a) shows an example extracted point set. However, only the point set are not enough to render a surface. To this end, each point was integrated into a 3D regular grid using our proposed MC algorithm [59], the overall effect of grid arrangement is shown in Fig. 4.16(b). A 3D plot of the grid is given in Fig. 4.16(c) and Fig. 4.16(d) shows the reconstructed plane of over 47,000 spatial points.

For each reconstructed point, the depth (z coordinates) was used for the purpose of evaluation only. The results are summarized in Table 4.1. The maximum error was 1.05 mm (obtained for group 1), while for the other groups, the errors were less than 1 mm. The average standard deviation was 0.26 mm while the mean of the error was 0.54 mm. As we observed in experiments, scanning gap is one of the factors that affect the reconstruction accuracy. Detecting laser points at such short distance is not usually used for the rigid endoscope in our situation.

Fig. 4.17 shows the error's fluctuations of the six group tests. We notice that the fluctuations were fewer when the scanning gap was 14-16 mm. That is why we scanned the surface using a scanning gap of 15 mm, which will be discussed in next section.

Though the scanning gaps were much smaller, our results demonstrate that the proposed system has a higher precision than what has been reported previously [57] in terms of planar reconstruction.

TABLE 4.1: Comparison of results of plane reconstruction.

Systems								Average
Hasegawa *et al.* [57]	Scanning gap [mm]	50	55	60	65	70		60
	Difference [mm]	0.52	0.73	0.85	1.14	**1.58**		**0.96**
	Standard deviation [mm]	0.31	0.48	0.53	0.71	**1.01**		**0.61**
	Proportion of error to distance [%]	1.04	1.33	1.42	1.75	2.26		
Our system	Scanning gap [mm]	10	12	14	16	18	20	15
	Difference [mm]	**1.05**	0.73	0.38	0.27	0.44	0.38	**0.54**
	Standard deviation [mm]	0.26	0.26	0.25	0.26	0.33	**0.20**	**0.26**
	Proportion of error to distance [%]	10.50	6.08	2.71	1.69	2.44	1.90	

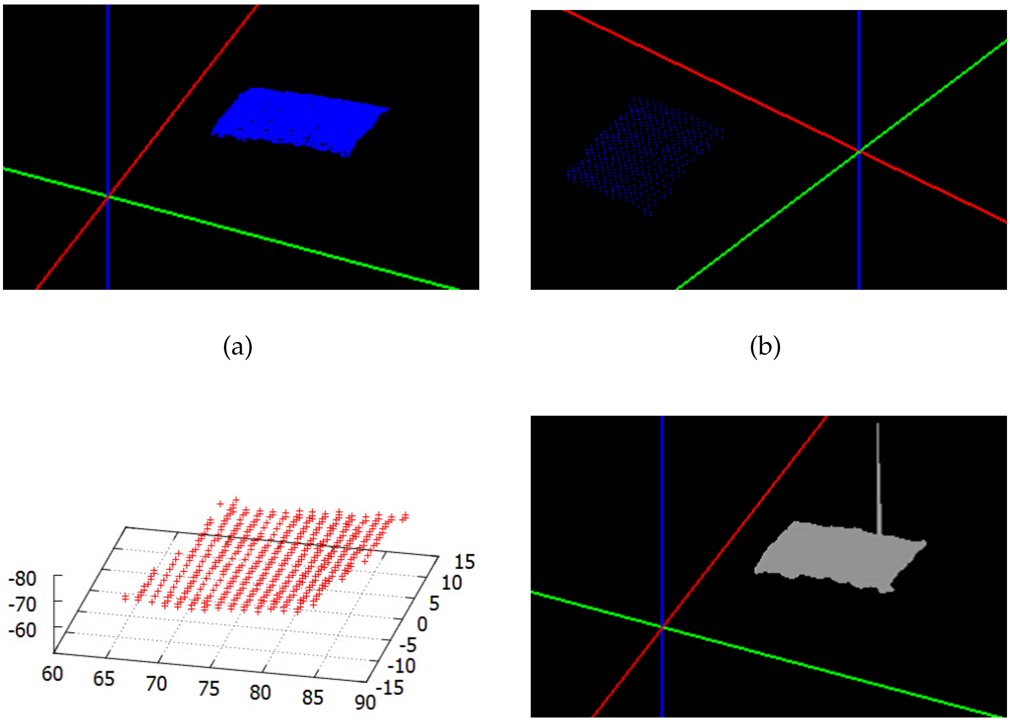

(a) (b)

(c) (d)

FIGURE 4.16: Reconstructed results of planar surface: (a) point set of a plane, (b) 3D grid arrangement, (c) plot of the obtained point set, and (d) reconstructed plane.

The comprehensive comparisons between our proposed system and other two endoscopic system are given in Table 4.2. We can notice that our system has the smallest size of the camera, baseline, and endoscopic tip. Although the system of Haneishi *et al.* [56] could get a high accuracy, the experiments were tested only in the air rather than under the water.

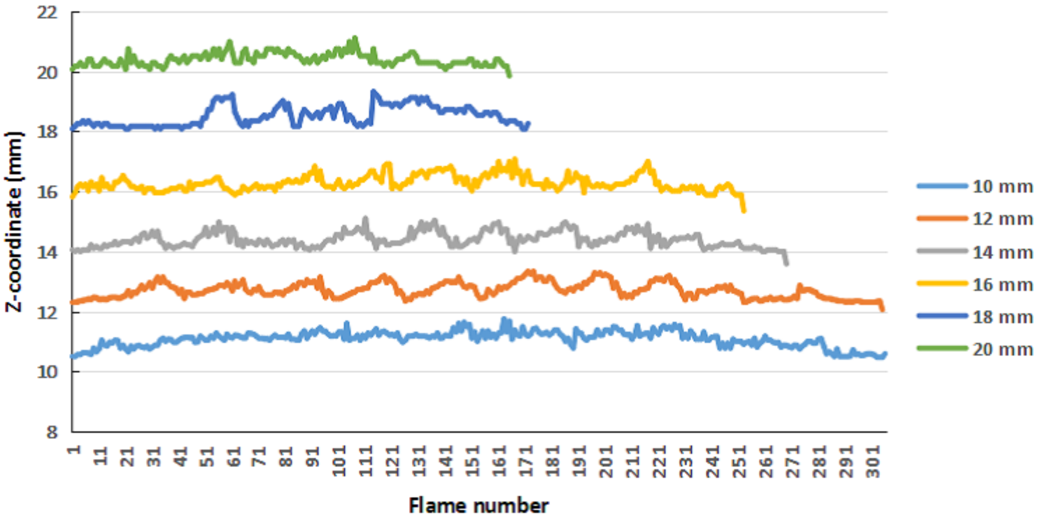

FIGURE 4.17: Depth value evaluation of planar surface.

TABLE 4.2: Comprehensive comparisons of endoscope systems (unit: mm). ‡ *Dia* means the size in diameter. † Environment is the experimental environment, that is in the air or in the water.

Endoscope systems	Haneishi *et al.* [56]	Hasegawa *et al.* [57]	Our system
Endoscopic tip	20 (*Dia*)	16 (*Dia*) ‡	8 (*Dia*)
Baseline	10	8.5	6
Camera	10.2 (*Dia*)	8 (*Dia*)	3.9 (*Dia*)
Scanning gap	10-20	50-70	10-20
Average error	0.05	0.96	0.54
Environment †	in the air	in the air	in the water

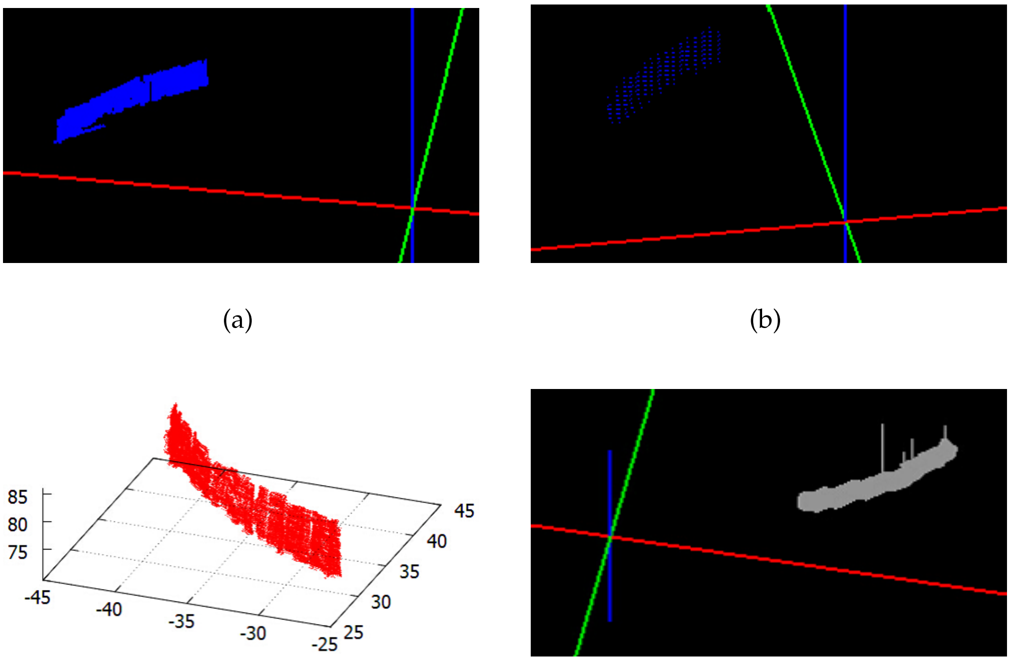

(a) (b)

(c) (d)

FIGURE 4.18: Experimental results of surface reconstruction using a cylindrical model. (a) Measured point cloud. (b) Reconstructed surface after vertex configuration. (c) 3D plot of the point set, and (d) Final reconstructed surface.

4.5.2 Reconstruction of Surface

For testing the performance of our system with regards to the surface reconstruction, a cylindrical model with a diameter of 49.1 mm was chosen as the object to be scanned. Because the aim of developing our endoscopic system was to make it operational in narrow spaces, we performed a partial scan of a small area on the surface of the model. The endoscope was moved around the surface of the cylinder using a scanning gap of 10-20 mm. The movement of the endoscope was controlled manually.

Fig. 4.18(a) shows the measured point cloud. A comparative method using the least squares fitting technique was employed to evaluate the accuracy of the surface reconstruction. The results revealed an average error of 2.425 mm that corresponded to a difference of 4.93% from the ideal diameter. It can be clearly

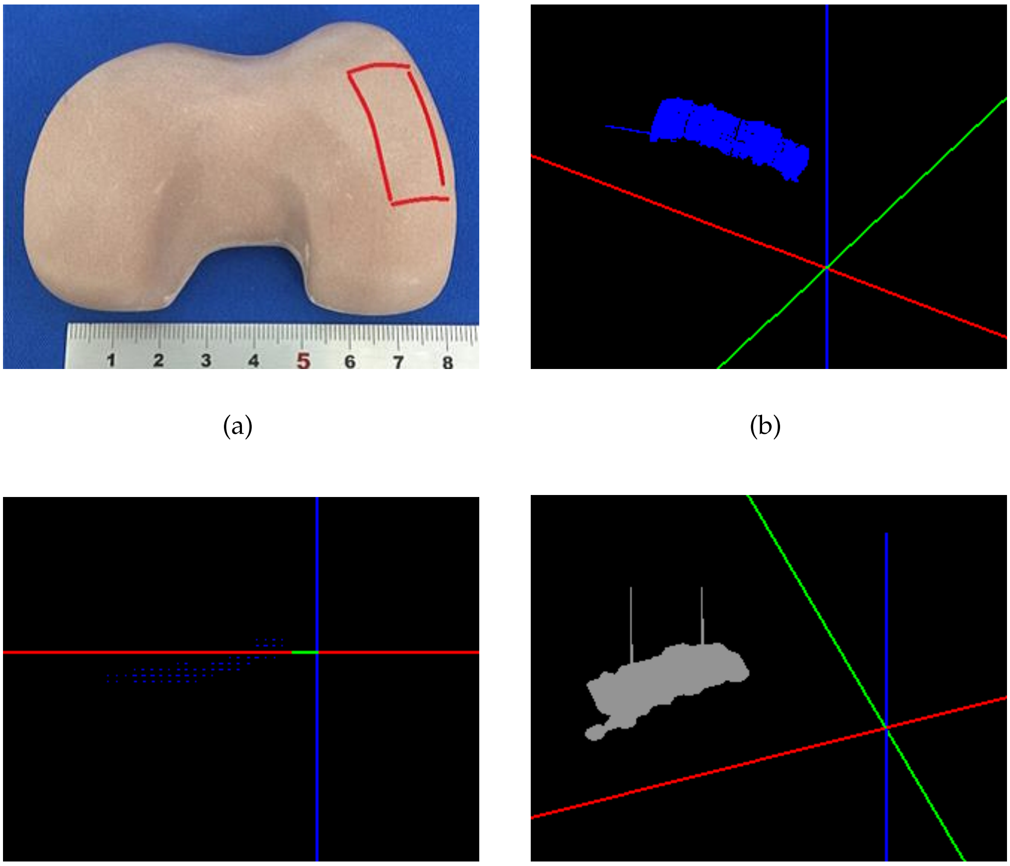

(a) (b)

(c) (d)

FIGURE 4.19: Results of 3D reconstruction of a normal-sized knee joint. (a) Photograph of the synthetic knee joint model with the scanned area marked by red lines. (b) Measured point cloud. (c) Reconstructed surface after vertex configuration, and (d) Final reconstructed surface.

observed in Fig. 4.18(b) that after the process of vertex configuration, most of the spatial points were arranged in a grid-like pattern. The 3D coordinates of the vertex are depicted in Fig. 4.18(c), and Fig. 4.18(d) displays the final reconstructed surface. It can be seen that the reconstructed shape is significantly similar to the original shape shown in Fig. 4.18(a).

For further evaluation of our endoscopic system, the second set of experiments using a synthetic knee joint were performed. A model of a knee joint of normal adult size was used for underwater testing. A specific area, referred

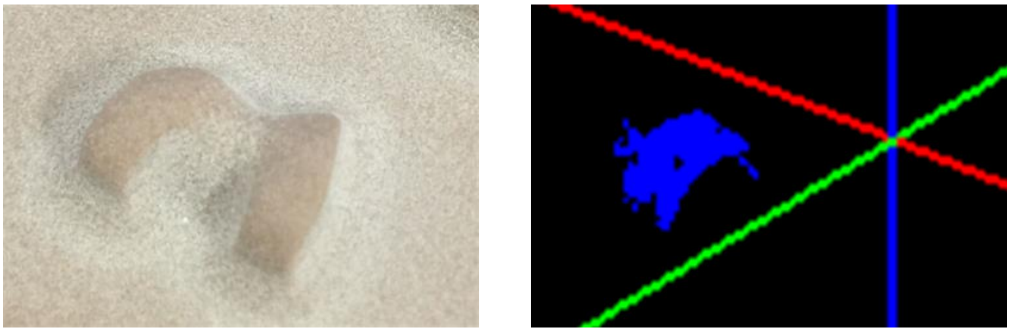

(a) (b)

FIGURE 4.20: 3D reconstruction results of a mini size knee joint: (a) mini size knee joint model and (b) its measured point cloud.

to as the donor site, from where a cartilage is harvested while performing mosaicplasty surgery [1], [2], [15], was selected as the object to be scanned. This area, approximately 25 × 10 mm in dimension, is marked in Fig. 4.19(a) by red lines. Fig. 4.19(b) shows the measured point cloud where the number of points is greater than 94,000. Fig. 4.19(c) illustrates the result of vertex configuration, and Fig. 4.19(d) displays the final reconstructed surface of the scanned area.

Because the width of the line laser passing through the optical fiber is extremely small (approximately 10 mm), a mini-sized synthetic knee joint model (9 mm × 6 mm × 2 mm) suitable for such a short line laser width was also tested for surface reconstruction using our endoscopic system. In this case, the entire surface of the model, shown in Fig. 4.20(a), was scanned. Fig. 4.20(b) depicts the 3D reconstructed point cloud. It is seen that a major portion of the surface is well reconstructed, including the radian of the joint surface on both sides.

4.5.3 Discussion

The precision of surface reconstruction is mainly affected by two factors in our system: the scanning gap and sensitivity to distance. Our results indicate that the endoscope can obtain a clear underwater image with a scanning gap of 20 mm or less. Detecting a line laser at such short distances is usually not possible in a rigid endoscope. As a result, perceiving the visual complexity of an image during underwater testing has become the main challenge that needs to be resolved. On the other hand, the proposed system differs from other reported endoscopic systems because of underwater surface reconstruction. The second parameter, sensitivity to distance depends mainly on the geometry of optical triangulation, especially on the length of the baseline [56], [75]. The shorter the baseline, the greater is the error in detecting the correct distance. Furthermore, it was observed that the fluctuation of the line laser in the proposed system had deteriorated compared to our previous system because of the shorter baseline (6 mm) in the former. Such a fluctuation occurs because the focal depth of our laser irradiation system is small [57]. The fluctuation can be decreased significantly by increasing the length of the baseline. However, the dimension of the endoscope tube cannot be increased beyond 8 mm for practical applications in real arthroscopic surgery.

Another factor that determines the accuracy is the intensity of the light source attached to the endoscope. A higher intensity will lead to a lower accuracy because of interference between the line laser and light source. The amount of missing data during arthroscopic surgery can easily reach up to 50% [76]. Hence, a DC power supply was employed to control the input voltage for the laser irradiation device in our system, since the interference can be decreased by adjusting the input voltage.

Indeed, vertex arrangement with the proposed MC algorithm is a problem in relation to the reconstructed outcome. Thus, a further investigation was then carried out. The data plotted in Fig. 4.21 were obtained by our MC algorithm.

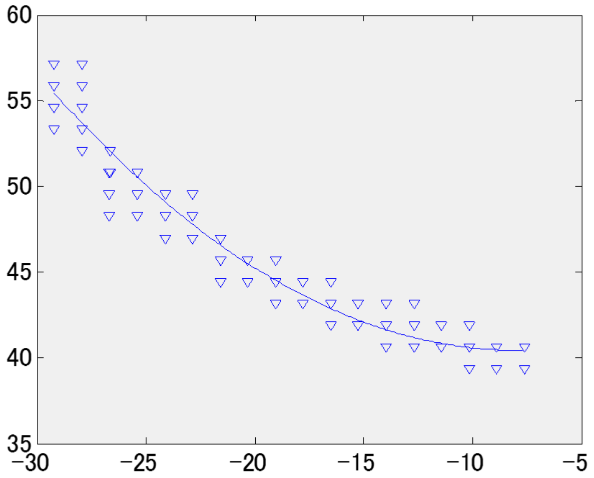

FIGURE 4.21: The fitting result of MC data.

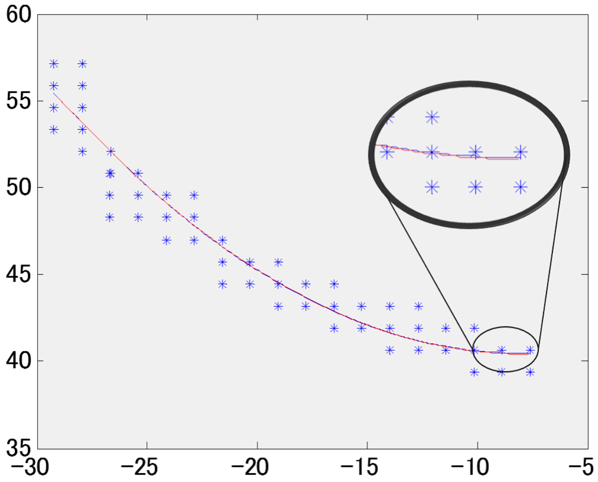

FIGURE 4.22: The fitting result of source data.

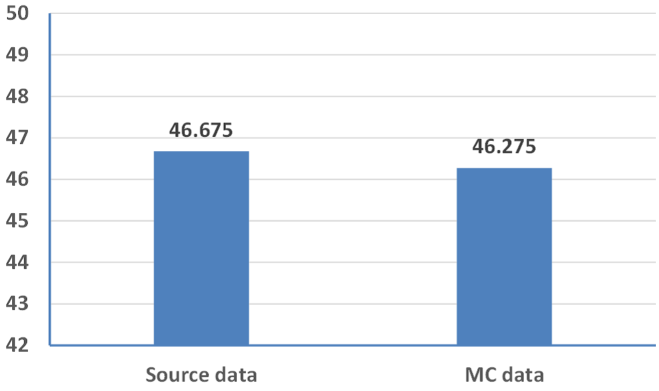

FIGURE 4.23: Comparison of fitting diameter.

Using these values and the LsF method, we found a best-fit curve of

$$y = 0.033x^2 + 0.518x + 42.450. \tag{4.18}$$

Another fitting curve based on the source data was also plotted with the MC data in one figure, the red curve in Fig. 4.22, whose best-fit equation is given by

$$y = 0.033x^2 + 0.536x + 42.624. \tag{4.19}$$

We can see that there were rarely differences, 0.4 mm difference in Fig. 4.23, between these two curve. The red curve was overlapped with the blue one (MC data).

In brief, the fitting result obtained from the source data is in line with those of using the proposed MC algorithm. The results posted here to confirm that our proposed MC algorithm does not affect or change the accuracy of the recovered surface.

4.6 Conclusion

In summary, we have developed an endoscopic system for underwater reconstruction of the knee joint surface . Although the accuracy of the proposed system is not as high as other endoscopic systems, in this study, we demonstrated the feasibility of our system to provide enhanced 3D information to surgeons during arthroscopic surgery. Our system can be especially useful for mosaicplasty surgery that is used for osteochondral transplantation in the knee. Navigating normal vectors during the surface reconstruction of the knee joint will be introduced in next chapter.

Chapter 5

3D Navigation of the Knee Joint Surface

5.1 Introduction

Osteochondral lesions of the knee are a common occurrence in athletic individuals. Such knee lesions result in increased focal contact pressure [32], [77], [78]. Without treatment, individuals may suffer from knee pain and the presence of joint effusion.

The mosaicplasty method, proposed by Hangody *et al.*, was first conceived in 1991 and subsequently applied in vigorous animal trials before clinical application the following year [79]. Since then, there have been a large number of case reports on the use of fresh autogenous cylindrical osteochondral grafts for the treatment of osteochondral lesions in the knee joint. In addition, over the last decade, the method has been introduced in the treatment of advanced defects in the elbow joint [80]–[83] . Fig. 5.1 illustrates an osteochondral transplantation, where one or more cylindrical osteochondral grafts from a non-weight-bearing side of the articular cartilage are harvested and subsequently implanted into the debrided defect area.

This type of procedure is not easy to accomplish, especially when performed using an arthroscopic technique. One of the crucial technical aspects of the mosaicplasty technique is the congruity of the cartilage thickness between the

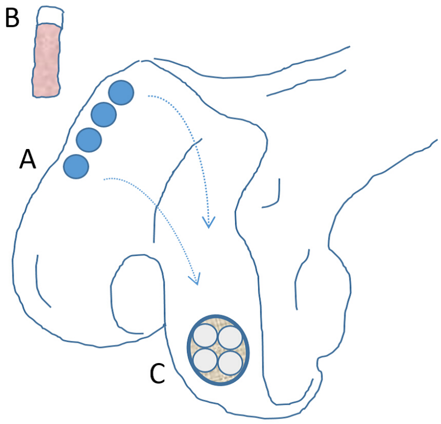

FIGURE 5.1: Schematic representation of osteochondral transplantation. A: Donor site. B: Cylindrical osteochondral graft. C: Osteochondral lesion area resurfaced with donor grafts.

donor and recipient [39]. Numerous case reports have been carried out to address this issue. Bobic *et al.* [4] pointed out that graft harvesting and insertion should be perpendicular to the articular surface, resulting in promising uniform results. Similarly, a clinical study [1] on the treatment of osteochondritis dissecans also emphasized that perpendicular access to the lesion is critical to maximizing the surface congruency in an open and arthroscopic technique. To avoid a potential pumping action and negative pressure in the depths of the recipient side, osteochondral grafts should be inserted flush with the knee joint surface [84]. With the rapid improvements in surgical technologies, newly designed mosaicplasty instrumentation has enabled minimal damage during graft harvesting, and has made graft insertion more precise and predictable. However, the perpendicular harvesting and insertion of grafts have been identified as a technically demanding aspect of the mosaicplasty technique.

As one of the most frequently performed minimally invasive surgeries, arthroscopic surgery has become a major trend in the areas of medical diagnosis and disease treatment. In general, an endoscope is inserted into the patient's body through a small incision to gain a direct view of the internal organ. Because an endoscope itself cannot provide a stereo visual view of the surgical target, it can be a difficult task to locate the six degrees of freedom (6DoF) of the endoscope

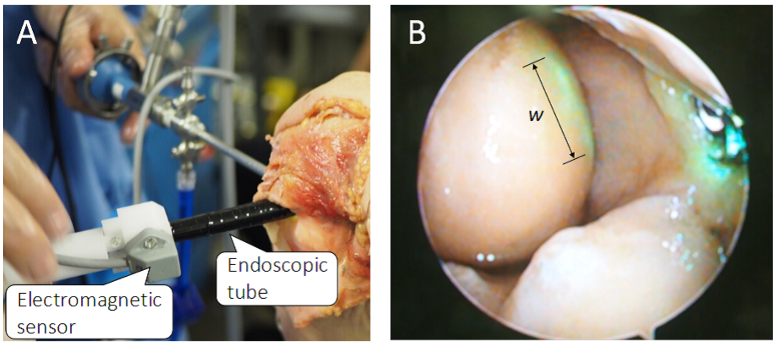

FIGURE 5.2: Experiment on a cadaveric knee joint: (A) insertion in a knee joint, and (B) femoral condyle and endoscopic tip. Here w indicates the width of the laser beam.

or harvester based on its position and orientation. Surgeons must therefore rely upon the motion parallax, object exclusion, and other indirect evidence of the depth to assess the spatial relationship of the objects [46].

The purpose of this chapter is to propose a specific navigation method for the rendering surface obtained using a 3D endoscopic system. Additionally, each location of the rendering surface can be navigated in the normal direction in real-time, which will allow the surgeons more precise and predictable operations when applying the mosaicplasty technique.

An experiment on a cadaveric knee joint was performed arthroscopically by a surgeon, the results of which illustrate the potential real-world application of the proposed system for use in minimally invasive surgery. An endoscopic tube can be inserted into the knee joint surface through a small incision, Fig. 5.2(A). In addition, an endoscopic tip is placed at a distance of approximately 15 mm in relation to the articular surface, Fig. 5.2(B).

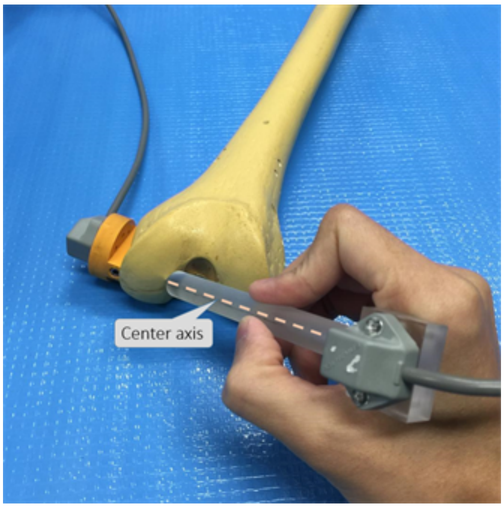

FIGURE 5.3: Current pose of the harvester tube.

5.2 Methodology

5.2.1 Normal Vector

As mentioned above, the optimal pose of the harvester should be perpendicular to the articular cartilage surface, that is the normal direction of the articular cartilage surface.

In our current study, the harvester used in experiment is somewhat different with that of medical application. Navigation using an imitation bone is illustrated in Fig. 5.3, current pose of the harvester is indicated by its central axis. It should be noted that 3D navigation experiments are performed in the water.

5.2.2 Calculation

For point set $\mathbb{R}^3$ located on the reconstructed surface, we need to compute its normal vector while the harvester is placed on the surface. As depicted in Fig. 5.4, point O is the current indicated position of the harvester tip, and vector $\boldsymbol{h}$ denotes the central axis of the harvester tube. Owing to the use of electromagnetic sensor 3 and the OpenGL technique, the 6DoF position and orientation of the harvester can be tracked and displayed continuously while the navigation

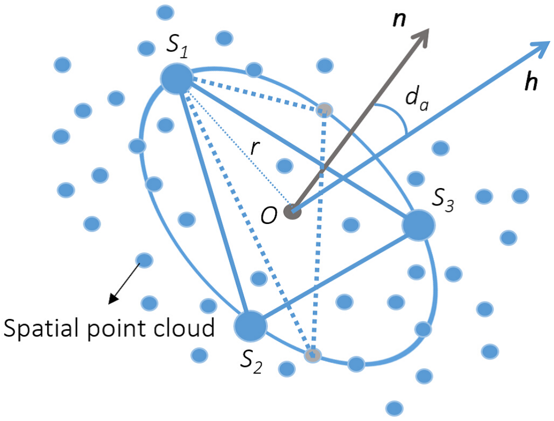

FIGURE 5.4: Calculation of a normal vector using an equilateral triangle inscribed in a circle. Improper triangle marked with a dotted line should be ignored.

process is activated. Parameter r is the circle radius and is designated as

$$r \in \left(1, \frac{w}{2}\right), \tag{5.1}$$

where w is the width of the laser beam.

Our objective is to find an equilateral triangle inscribed in a given circle, whose radius is defined by r. In addition, all apexes of the triangle are located on $\mathbb{R}^3$. The cross product of two arbitrary vectors built by the triangle is then the normal direction corresponding to the current point. The setting of r may affect the precision of the normal vector mathematically. In this case, we finally set r as small as possible (r = 1-3 mm).

Let $S^k_{i,\mathbf{w}} = \{S_1, S_2, S_3\} \in \mathbb{R}^3$ be the world coordinates of the apexes. The normal vector of the current point can then be calculated as

$$\boldsymbol{n} = \overrightarrow{S_1S_2} \times \overrightarrow{S_2S_3}, \tag{5.2}$$

where the inclined angle is $\frac{\pi}{3}$ in our case.

In our system, the angle difference is displayed in real time to assist the surgeon in adjusting the harvester pose. The angle d_a between vector $\boldsymbol{n}$ and $\boldsymbol{h}$ is express as

$$d_a = \langle \boldsymbol{n}, \boldsymbol{h} \rangle = \arccos\Big(\frac{\boldsymbol{n} \cdot \boldsymbol{h}}{||\boldsymbol{n}||||\boldsymbol{h}||}\Big). \tag{5.3}$$

For a brief display on the navigation screen, we unitize the normal vector as follows:

$$\hat{\boldsymbol{n}} = \begin{cases} \dfrac{\boldsymbol{n}}{||\boldsymbol{n}||}, & (\text{if } \boldsymbol{n} \neq \mathbf{0}), \\ \\ \hat{\boldsymbol{k}}, & (\text{otherwise}), \end{cases} \tag{5.4}$$

where $\hat{\boldsymbol{k}}$ is a unit vector in the depth direction of the point set for $\boldsymbol{n} = \mathbf{0}$, which is used for avoiding bugs from a programming perspective. In fact, experiments have showed that we can consistently find a triangle that consists of three points on the surface of interest, and thus the normal vector does not fall into a zero vector. Our approach for computing the normal vector $\hat{\boldsymbol{n}}$ is summarized in Algorithm 1.

Algorithm 1: Navigating a normal vector for reconstructed surface

```
Input  : Point set $\mathbb{R}^3$ and harvester pose $h$;
Output: Normal vector $\hat{n}$ and angle difference $d_a$;
Set width of the laser beam $w$, circle radius $r$, (Eq. 5.1);
for $m = 0$ to $N$ ($N$: total number of points) do
    if $r \in (1, \frac{w}{2})$ then
        Save the first point $S_1$;
    end
    if $||\overrightarrow{S_1S_2}|| \in (\sqrt{3}, \frac{\sqrt{3}w}{2})$ then
        Save the second point $S_2$;
    end
    if both $||\overrightarrow{S_2S_3}||$ and $||\overrightarrow{S_3S_1}|| \in (\sqrt{3}, \frac{\sqrt{3}w}{2})$ then
        Save the third point $S_3$;
    end
    Generate an equilateral triangle;
end
Compute cross product of $\overrightarrow{S_1S_2}$ and $\overrightarrow{S_2S_3}$, (Eq. 5.2);
Compute the included angle between $n$ and $h$, (Eq. 5.3);
Unitize vector $n$, (Eq. 5.4);
return $\hat{n}$ and $d_a$;
```

5.3 Underwater Experimental Results

5.3.1 Precision Evaluation

A validation cylinder with a diameter of 50.0 mm was used to estimate the system's 3D navigation. A preliminary adjustment of the laser brightness was needed prior to the data collection. A portion of the surface of the cylinder was then scanned using the endoscope, and 30 spots on the surface whose real normal directions were marked in advance were measured using the harvester tip. The central axis of the harvester overlapping the real normal direction is considered the optimal angle/pose. It should be noted that both the underwater reconstruction and navigation experiments were conducted by the same person, who is not a professional surgeon.

5.3.2 Statistical Analysis

All data are presented in terms of Mean ± SD. The navigation results were compared with those of two groups applying a freehand technique [30] using a comparison of means (t - test). For all tests, when $P < 0.05$, the two means are considered significantly different. A statistical analysis was conducted using a MedCalc, version 16.1 statistical software package (MedCalc Software, Ostend, Belgium).

The experimental results show that our system has an average navigation error of 9.5° within the range of 5° to 17°, with an SD of 2.86°. In contrast, the errors for two sites when applying a freehand technique during arthroscopic surgery were 14.8° within the range of 6° to 26° (SD of 7.53°), and 12.6° within the range of 4° to 17° (SD of 3.98°). A statistical analysis showed a significant difference ($P = 0.001$ and $P = 0.0024$) between the navigated technique (N = 30) and freehand technique (N = 20), as depicted in Fig. 5.5.

In order to show the system performance, Fig. 5.6 summarizes the time consumption of each process. It just took 1.47 s on average to scan a 200 mm^2 surface. Further more, displaying the recovered surface with our proposed MC

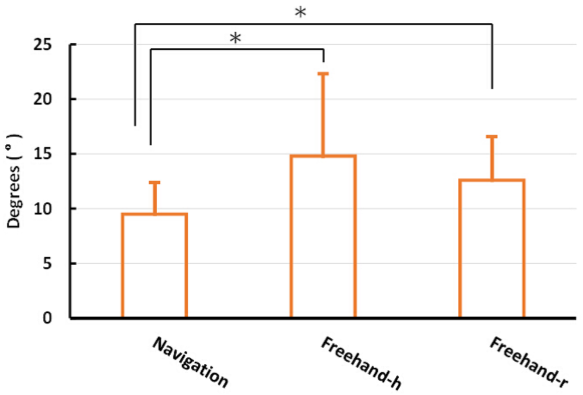

FIGURE 5.5: Angle comparison between proposed navigation technique and freehand technique. Group *Freehand-h* represents the data of a graft harvest, and *Freehand-r* represents the data of a recipient site coring. The asterisk indicates that there is a significant difference in the data.

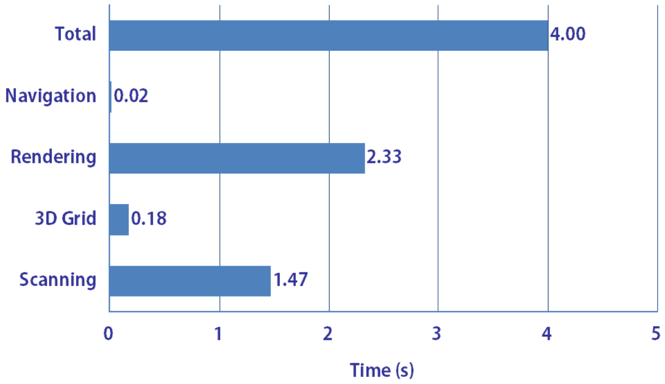

FIGURE 5.6: System performance.

algorithm is quite fast (2.41 *s*), which includes the 3D grid processing and the surface rendering. The time of navigation indicates the application response time. Summarily, this endoscopic system takes the surgeon only 4.4 *s* to get the 3D navigation information.

Figure 5.7 shows an example of a navigated normal vector of a synthetic femoral bone (Zimmer K.K. Inc., Japan). Auto-grafts have been generally used to treat smaller (<200 mm^2) full-thickness chondral defects [85]. Thus, the red lines in Fig. 5.7(a) mark an area that was scanned in water. Using the OpenGL technique, the reconstructed surface was rendered and displayed based on the electrical center of sensor 2, which was attached to the object that was scanned.

Fig. 5.7(b) depicts the measured point cloud while scanning the bone surface. It can be observed in Fig. 5.7(c) that after the process of vertex configuration, the spatial points were arranged in a grid-like patten. Fig. 5.7(d) shows the final reconstructed surface of the scanned area.

The navigation process would start immediately when the 'Navi' button was clicked. Once the harvester was placed on the bone surface, current pose, as well as a normal vector, were displayed continuously, see Fig. 5.7(e). During navigation, we can move the harvester to choose a certain place where we want to investigate. Furthermore, different viewpoints are available by controlling the Form of CamePos, Fig. 5.7(f). Pose adjustment shown in Fig. 5.7(g) indicates that the angle between the normal vector and harvester is 2 degree. When the harvester was overlapping the normal vector, the screen would output an angle difference (AngDif) of 0 degrees, Fig. 5.7(h).

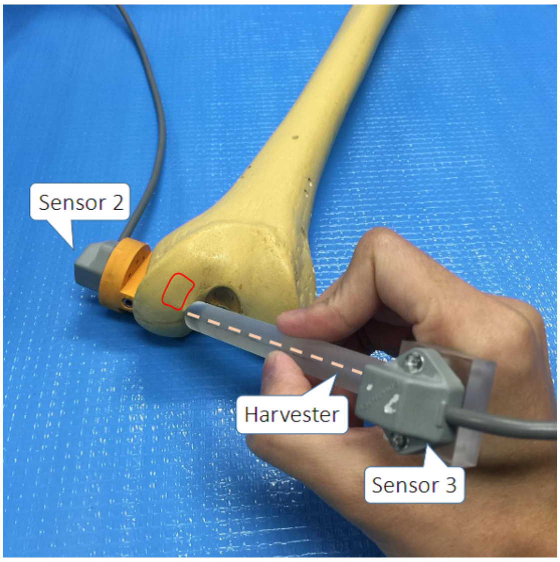

(a) Photograph of the femoral bone. The red lines mark the area that was scanned in the experiment.

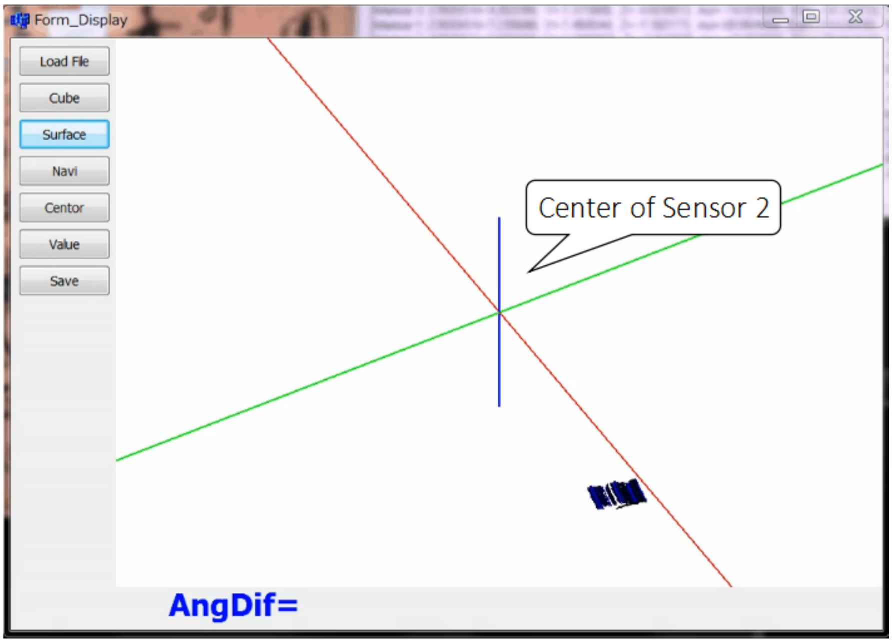

(b) The surface was scanning and its measured pint cloud.

FIGURE 5.7: Examples of 3D navigation of imitation bone surface.

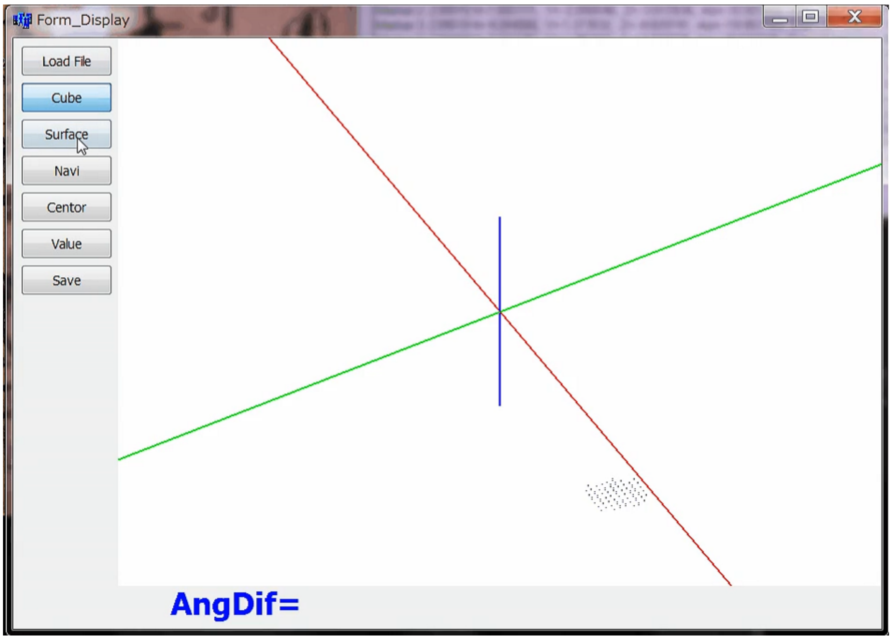

(c) Reconstructed surface after vertex configuration and then the 3D grid is generated.

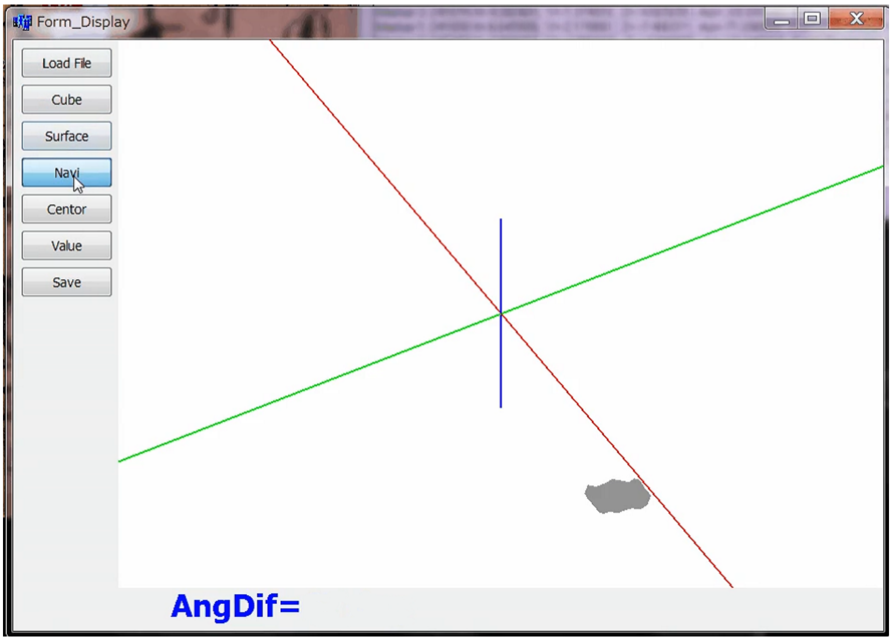

(d) Final reconstructed surface.

FIGURE 5.7: (Continued).

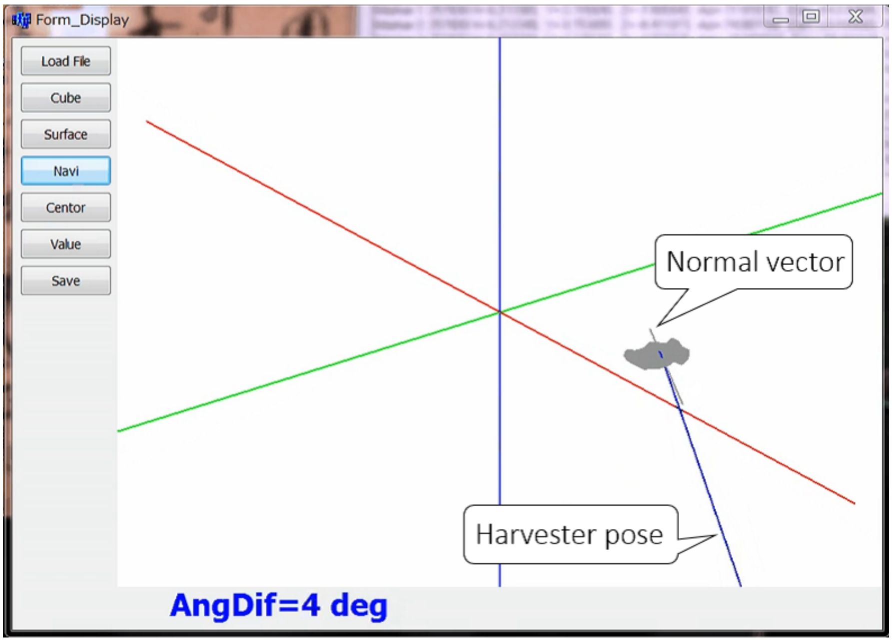

AngDif=4 deg

(e) The normal vector and current pose were displayed immediately when the harvester was placed on the surface. 'AngDif' indicates the angle difference in degree.

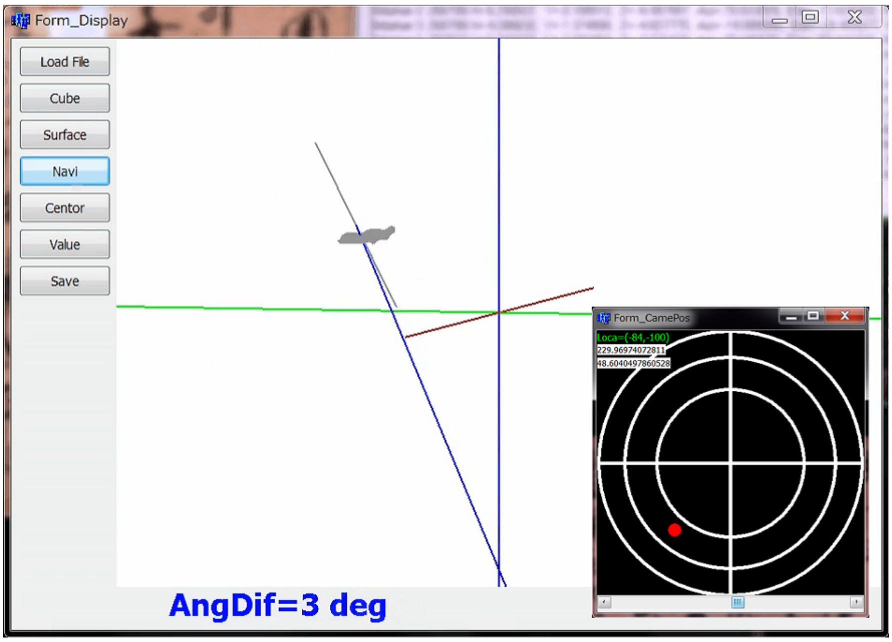

Loca=(-84,-100)
229.96974072811
48.6040497860528

AngDif=3 deg

(f) Pose adjustment of the harvester. Currently, error is 3 degree. Viewpoint can be changed with the aid of CamePos.

FIGURE 5.7: (Continued).

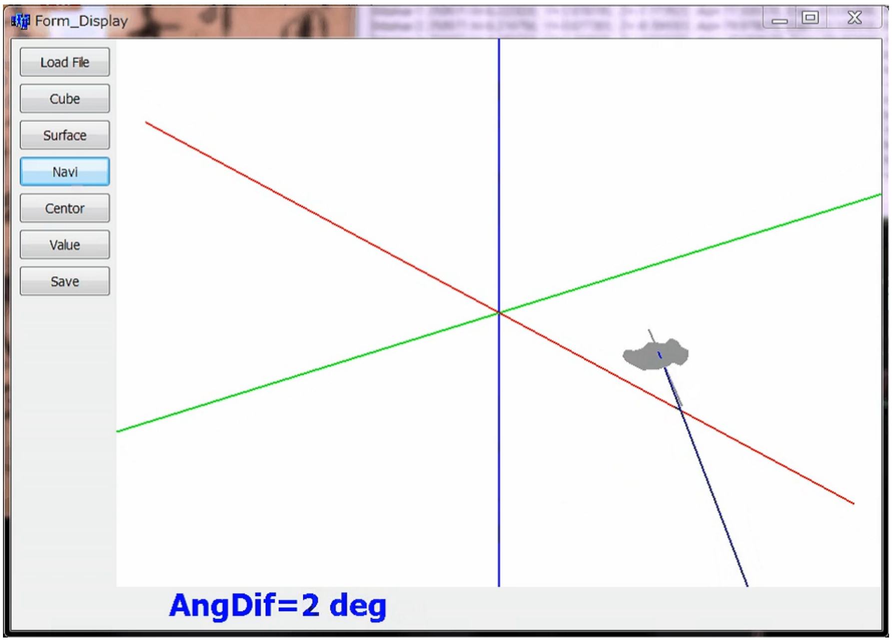

(g) Pose adjustment of the harvester. Currently, error is 2 degree.

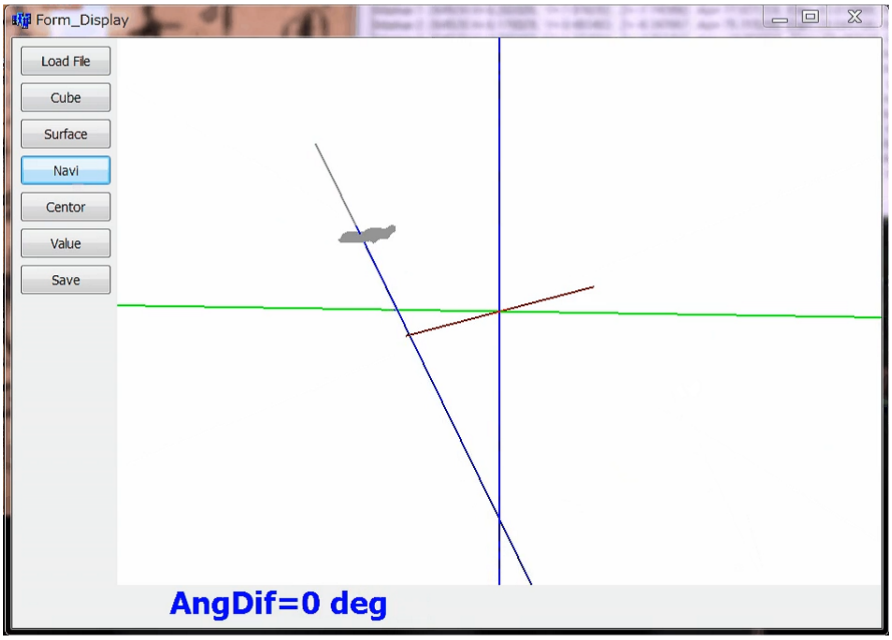

(h) Optimal pose of the harvester. The harvester was overlapping the computed normal vector.

FIGURE 5.7: (Continued).

5.3.3 Discussion

Osteochondral lesions are a common sports-related injury for which osteochondral autograft transplantation (OAT) is a popular method of treatment. Although computer-assisted arthroscopic techniques have increased considerably recently, OAT of the knee joint performed with navigation technique is very few.

An open surgical technique [32] and a minimally invasive surgery arthroscopic approach [30] were both reported by P. D. Benedetto *et al*. In their studies, a conventional image-free navigation system (Praxim, La Tronche, France) was used in combination with an osteochondral autograft transplantation system (OATS, Arthrex, Florida, USA). Navigated arthroscopic mosaicplasty for osteochondral lesions in a cadaveric model ensures a permanent visualization of the angle of graft removal and placement. However, the limitations of this system mainly include the use of invasive intra-osseous reference markers and a preliminary fixation of a marker to the instrumentation of the guide system. Critically, the former is viewed as giving further harm to the patient's knee. Hence, it is meaningful for the minimally invasive surgery to navigate a knee joint surface without any invasive instrumentation [86].

In our system, owing to the use of an electromagnetic device, the position and orientation of the harvester can be accurately tracked, and each point located on the reconstructed surface of the knee joint can be used to generate a normal vector in real time using our proposed method. A smaller circle radius can improve the calculation accuracy of a normal vector and hence the accuracy of 3D navigation; however, the main source of errors during navigation is the 3D recovery of the surface. Difficulties remaining in the surface recovery include an inter-reflection of the light source and non-uniform reflectance property of the surface of the knee joint.

The general limitations of the proposed navigation system are mainly a consequence of a lack of *in vivo* experiments. A limited number of models were tested for an accuracy evaluation. A further limitation of our study is insufficient accuracy comparisons with other 3D navigation systems. An accuracy comparison between the navigated and freehand techniques was assessed under the assumption that the accuracy evaluated using a validation cylinder was equal to that of a clinical application. A different analytic method, such as a 3D navigation analysis or a custom-made knee joint model, may be required for an exact accuracy assessment of the navigation procedure.

5.4 Conclusion

We proposed a practical approach to navigating a 3D normal vector of a knee joint surface. Our method enables the selection of optimal points based on an electromagnetic sensor, which can measure the 6DoF position and orientation of the harvester. During the navigation, the harvester can be identified and precisely located, which is expected to guide surgeons in their decision-making. The results from a knee joint model have confirmed the feasibility of achieving 3D navigation. Compared to the results of a freehand technique performed during actual surgery, the navigation accuracy from using our proposed system was significantly improved from at least 12.6° to 9.5°. In addition, the small diameter (8 mm) of our endoscope makes it extremely convenient for application in a narrow space.

Chapter 6

Conclusions

This thesis addressed the issue of stereoscopic visualization and navigation of the knee joint surface in a narrow operating space. The stereo visual of the surgical target is crucial to ensure surgeons depth perception during knee arthroscopic surgery. Currently, conventional endoscope-based arthroscopic surgery does not provide stereoscopic information to the surgeon. Accordingly, surgeons can only view the operation field via a video monitor on which 2D information of the surgical target is displayed. Under such circumstance, assessing the spatial relationship of the objects is a troublesome task. An attempt to solve this problem, a fiber-based endoscopic system was developed and capable of 3D imaging the surface of the knee joint underwater in real time. Moreover, this system also can navigate a normal vector for the reconstructed surface which seeks to provide the surgeon with more precise and predictable operation.

The endoscopic tip and graphical user interface (GUI) were concurrently developed. There are several different sizes of the endoscopic tip were designed and evaluated. The final design of the endoscopic tip was the smallest diameter, which is 8 mm that suitable to apply in the knee arthroscopic surgery. This size was chosen based on the diameter of the incision is 10 mm or less.

Experiments to reconstruct the surface of the knee joint were conducted in air using a camera of 7.0 mm diameter. These experiments were performed to investigate the correlation between the length of the baseline and the reconstructed accuracy. The results revealed that the quality of laser point detection improved when the deviation angle of the line laser with respect to the optical axis was 14° in case that the baseline was 6 mm. Based on the results, it was assumed that the deviation angle of the line laser could be achieved by using a prism.

The obtained point cloud differ greatly from those of computed tomography (CT) or magnetic resonance imaging (MRI). Without using a specific vertex configuration algorithm, the point cloud is not able to render and the isosurface can not be extracted. To overcome this limitation, a specific vertex processing has been developed. The proposed marching cubes (PMC) algorithm was introduced in extenso and applied in vertex processing. The experimental results showed that the cubic interval being 1.27 mm could obtain a smooth rendered surface. Further, a comparison of source data and MC data demonstrated that the PMC method did not change the accuracy of the reconstructed surface.

Tacking into consideration fact that arthroscopic surgery is usually operated with flowing water, a set of underwater experiments were performed using a smaller camera and prism for further evaluation. Reconstruction of planar surface revealed that the system has an average measurement error of 0.54 mm with the mean of standard deviation being 0.26 mm. A comparative method using the least squares fitting was employed to assess the accuracy of the surface reconstruction. The results showed an average error of 2.425 mm that corresponded to a difference of 4.93% from the ideal diameter; assuming those of the knee joint surface are the same.

In navigation experiments, a specific navigation approach suitable for use in a rendered surface was presented. An experiment of navigating a normal vector using a femoral bone was performed under water. Each location of the rendering surface can be navigated by the harvester and displayed on the GUI, the surgeon can easily adjust the pose of the instrumentation based on the displayed navigation info. The experimental results show that our system has an average navigation error of 9.5° within the range of 5° to 17°, with an SD of 2.86°. In contrast, the errors for two sites when applying a freehand technique during arthroscopic surgery were 14.8° within the range of 6° to 26° (SD of 7.53°), and 12.6° within the range of 4° to 17° (SD of 3.98°). A statistical analysis showed a significant difference (P = 0.001 and P = 0.0024) between the navigated technique (N = 30) and freehand technique (N = 20).

To conclude, the fiber-based endoscopic system has been developed successfully and used to investigate the 3D visualization and navigation of the knee joint surface in real time. Current study illustrates that the endoscopic system has a potential of the medical application. Whereas, the accuracy obtained were affected by a few limitations depicted later in this chapter. Hence, further research may provide a more reliable answer to the current issues.

6.1 Limitations

Current study was conducted carefully, however, there are some limitations that might affect the results we obtained. Among the limitations are:

i. The experiments of this study were performed in the laboratory environment, and the imitation bone models were cleaned before doing the experiments. Furthermore, a few factors that affect the laser points extraction do not include in the current study. For example, the soft-tissue and blood, which is a consequence of missing data during the practical application in real arthroscopic surgery.

ii. The current system is mainly a consequence of the lack of *in vivo* experiments due to the missing data are high during arthroscopic surgery.

iii. In the experiment of 3D navigation, accuracy comparison with other 3D navigation system is insufficient.

iv. The display form is not enough for the orientation adjusting of the harvester.

6.2 Future Works

The present research can be further expanded in the near future by improving some of the issues encountered. The list of possible enhancements includes:

i. Improve the pattern of laser or change another irradiation pattern to increase the stability of the system.
ii. Scan the surface of the knee joint with a smaller scanning gap, e.g., 5-8 mm, which is a suggestion proposed by a surgeon.
iii. Perform the experiment using cadaveric bone such as the femoral bone of the rabbit to assess the capability of the developed system.
iv. A different analytic method that evaluates the accuracy of 3D navigation may be required.
v. Increase the test number of the experiment of 3D navigation to increase the reliability of the system accuracy.
vi. Add three forms to show the normal vector from the view points of different axes.

Appendix A

List of Publication

A.1 Academic Journals

[1] **Zhongjie Long** and Kouki Nagamune, "A Marching Cubes Algorithm: Application for Three-dimensional Surface Reconstruction Based on Endoscope and Optical Fiber", *Information*, Vol. 18, No. 4, pp. 1425-1437, 2015.

[2] **Zhongjie Long** and Kouki Nagamune, "Underwater 3D Imaging Using a Fiber-Based Endoscopic System for Arthroscopic Surgery", *Journal of Advanced Computational Intelligence and Intelligent Informatics*, Vol. 20, No. 3, pp. 448-454, 2016.

[3] **Zhongjie Long**, Shogo Kawaguchi, and Kouki Nagamune, "Development of Manual Measurement System with Stereo Markers for Lachman Test", *Journal of Advanced Computational Intelligence and Intelligent Informatics*, Vol. 20, No. 3, pp. 385-392, 2016.

[4] **Zhongjie Long**, Kouki Nagamune, Ryosuke Kuroda, and Masahiro Kurosaka, "Real-time 3D Visualization and Navigation Using Fiber-based Endoscopic System for Arthroscopic Surgery", *Journal of Advanced Computational Intelligence and Intelligent Informatics*. Vol. 20, No. 5, pp. 735-742, 2016.

A.2 International Conferences

[1] **Zhongjie Long**, Kouki Nagamune, Xiaoli Xu, et al., "Real-time 3D Reconstruction of Endoscopy and Microfiber Line Laser", *In Proceedings of* 5^{th} *International Symposium on Test Automation & Instrumentation (ISTAI)*, pp. 262-267, Beijing, China, 2014.

[2] **Zhongjie Long** and Kouki Nagamune, "Underwater Surface Reconstruction of Narrow Space by Endoscope and Optical Fiber: Application to Minimally Invasive Surgery", *Poster session presented at* 37^{th} *IEEE International Conference of Engineering in Medicine and Biology Society (EMBC)*, 2015 Aug 29th, Milan, Italy.

[3] **Zhongjie Long** and Kouki Nagamune, "3D Tracking System Using Endoscope for Narrow Space", *Poster session presented at* 38^{th}*IEEE International Conference of Engineering in Medicine and Biology Society (EMBC)*, 2016 Aug 19th, Orlando, USA.

[4] **Zhongjie Long**, Kouki Nagamune, and Xiaoli Xu, "A Graphical User Interface for Real-time Display", *In Proceedings of* 6^{th} *International Symposium on Test Automation & Instrumentation (ISTAI)*, pp. 89-92, Beijing, China, 2016.

Bibliography

[1] L. Hangody, G. Kish, Z. Kárpáti, and R. Eberhart, “Osteochondral plugs: autogenousosteochondral mosaicplasty for the treatment of focal chondral and osteochondral articular defects”, *Operative Tech. in Orthopaedics*, vol. 7, no. 4, pp. 312–322, 1997.

[2] Y. Matsusue, T. Yamamuro, and H. Hama, “Arthroscopic multiple osteochondral transplantation to the chondral defect in the knee associated with anterior cruciate ligament disruption”, *Arthroscopy: The Journal of Arthroscopic & Related Surgery*, vol. 9, no. 3, pp. 318–321, 1993.

[3] L Hangody, I Szigeti, Z Karpati, and L Sukosd, “A new method for the treatment of serious localized cartilage damage in the knee joint”, *Osteoporos Int*, vol. 3, pp. 106–114, 1996.

[4] V Bobić, “Arthroscopic osteochondral autograft transplantation in anterior cruciate ligament reconstruction: a preliminary clinical study”, *Knee Surgery, Sports Traumatology, Arthroscopy*, vol. 3, no. 4, pp. 262–264, 1996.

[5] N. T. Clancy, D. Stoyanov, G.-Z. Yang, and D. S. Elson, “An endoscopic structured lighting probe using spectral encoding”, in *European Conferences on Biomedical Optics*, International Society for Optics and Photonics, 2011, pp. 809 002–809 002.

[6] N. Hernes, A Toril, F. Lindseth, T. Selbekk, A. Wollf, O. V. Solberg, E. Harg, O. M. Rygh, G. A. Tangen, I. Rasmussen, *et al.*, “Computer-assisted 3d ultrasound-guided neurosurgery: technological contributions, including multimodal registration and advanced display, demonstrating future perspectives”, *The International Journal of Medical Robotics and Computer Assisted Surgery*, vol. 2, no. 1, pp. 45–59, 2006.

[7] J. Hummel, M. Figl, M. Bax, H. Bergmann, and W. Birkfellner, “2d/3d registration of endoscopic ultrasound to ct volume data”, *Physics in medicine and biology*, vol. 53, no. 16, pp. 4303–4316, 2008.

[8] D. Hong, W. Tavanapong, J. Wong, J. Oh, and P. C. De Groen, “3d reconstruction of virtual colon structures from colonoscopy images”, *Computerized Medical Imaging and Graphics*, vol. 38, no. 1, pp. 22–33, 2014.

[9] X. Luo, Y. Wan, X. He, and K. Mori, “Adaptive marker-free registration using a multiple point strategy for real-time and robust endoscope electromagnetic navigation”, *Computer methods and programs in biomedicine*, vol. 118, no. 2, pp. 147–157, 2015.

[10] M. S. Nosrati, R. Abugharbieh, J.-M. Peyrat, J. Abinahed, O. Al-Alao, A. Al-Ansari, and G. Hamarneh, "Simultaneous multi-structure segmentation and 3d nonrigid pose estimation in image-guided robotic surgery", *IEEE transactions on medical imaging*, vol. 35, no. 1, pp. 1–12, 2016.

[11] E. Hohmann and K. Tetsworth, "Large osteochondral lesions of the femoral condyles: treatment with fresh frozen and irradiated allograft using the mega oats technique", *The Knee*, vol. 23, no. 3, pp. 436–441, 2016.

[12] F. T. Blevins, J. R. Steadman, J. J. Rodrigo, and J. Silliman, "Treatment of articular cartilage defects in athletes: an analysis of functional outcome and lesion appearance.", *Orthopedics*, vol. 21, no. 7, pp. 761–7, 1998.

[13] C. S. Ahmad, Z. A. Cohen, W. N. Levine, G. A. Ateshian, and V. C. Mow, "Biomechanical and topographic considerations for autologous osteochondral grafting in the knee", *The American journal of sports medicine*, vol. 29, no. 2, pp. 201–206, 2001.

[14] D. Araki, R. Kuroda, T. Matsumoto, K. Nagamune, T. Matsushita, S. Kubo, Y. Oniki, and M. Kurosaka, "An analysis of surface profile for cylindrical osteochondral grafts of the knee quantitative evaluation using a three-dimensional laser scanner", *Knee Surgery, Sports Traumatology, Arthroscopy*, vol. 21, no. 8, pp. 1794–1800, 2013.

[15] M. Brittberg, A. Lindahl, A. Nilsson, C. Ohlsson, O. Isaksson, and L. Peterson, "Treatment of deep cartilage defects in the knee with autologous chondrocyte transplantation", *New england journal of medicine*, vol. 331, no. 14, pp. 889–895, 1994.

[16] W. W. Curl, J. Krome, E. S. Gordon, J. Rushing, B. P. Smith, and G. G. Poehling, "Cartilage injuries: a review of 31,516 knee arthroscopies", *Arthroscopy: The J. of Arthroscopic & Related Surgery*, vol. 13, no. 4, pp. 456–460, 1997.

[17] W Widuchowski, J Widuchowski, and T Trzaska, "Articular cartilage defects: study of 25,124 knee arthroscopies", *The Knee*, vol. 14, no. 3, pp. 177–182, 2007.

[18] M. Marcacci, G. Filardo, and E. Kon, "Treatment of cartilage lesions: what works and why?", *Injury*, vol. 44, S11–S15, 2013.

[19] A. E. Gross, N. Shasha, and P. Aubin, "Long-term followup of the use of fresh osteochondral allografts for posttraumatic knee defects.", *Clinical orthopaedics and related research*, vol. 435, pp. 79–87, 2005.

[20] A. Hennig and J. Abate, "Osteochondral allografts in the treatment of articular cartilage injuries of the knee", *Sports medicine and arthroscopy review*, vol. 15, no. 3, pp. 126–132, 2007.

[21] P. C. McCulloch, R. W. Kang, M. H. Sobhy, J. K. Hayden, and B. J. Cole, "Prospective evaluation of prolonged fresh osteochondral allograft transplantation of the femoral condyle minimum 2-year follow-up", *The American journal of sports medicine*, vol. 35, no. 3, pp. 411–420, 2007.

[22] B. G. Ochs, C. Müller-Horvat, D. Albrecht, B. Schewe, K. Weise, W. K. Aicher, and B. Rolauffs, "Remodeling of articular cartilage and subchondral bone after bone grafting and matrix-associated autologous chondrocyte implantation for osteochondritis dissecans of the knee", *The American journal of sports medicine*, vol. 39, no. 4, pp. 764–773, 2011.

[23] D. Pape, G. Filardo, E. Kon, C. N. van Dijk, and H. Madry, "Disease-specific clinical problems associated with the subchondral bone", *Knee Surgery, Sports Traumatology, Arthroscopy*, vol. 18, no. 4, pp. 448–462, 2010.

[24] K. Schlichting, H. Schell, R. U. Kleemann, A. Schill, A. Weiler, G. N. Duda, and D. R. Epari, "Influence of scaffold stiffness on subchondral bone and subsequent cartilage regeneration in an ovine model of osteochondral defect healing", *The American journal of sports medicine*, vol. 36, no. 12, pp. 2379–2391, 2008.

[25] B. Dozin, M. Malpeli, R. Cancedda, P. Bruzzi, S. Calcagno, L. Molfetta, F. Priano, E. Kon, and M. Marcacci, "Comparative evaluation of autologous chondrocyte implantation and mosaicplasty: a multicentered randomized clinical trial", *Clinical Journal of Sport Medicine*, vol. 15, no. 4, pp. 220–226, 2005.

[26] G. Kordás, J. S. Szabó, and L. Hangody, "Primary stability of osteochondral grafts used in mosaicplasty", *Arthroscopy: The Journal of Arthroscopic & Related Surgery*, vol. 22, no. 4, pp. 414–421, 2006.

[27] M. Marcacci, E. Kon, M. Delcogliano, G. Filardo, M. Busacca, and S. Zaffagnini, "Arthroscopic autologous osteochondral grafting for cartilage defects of the knee prospective study results at a minimum 7-year follow-up", *The American journal of sports medicine*, vol. 35, no. 12, pp. 2014–2021, 2007.

[28] A. H. Gomoll, J. Farr, S. D. Gillogly, J Kercher, and T. Minas, "Surgical management of articular cartilage defects of the knee", *J Bone Joint Surg Am*, vol. 92, no. 14, pp. 2470–2490, 2010.

[29] T. S. Lynch, R. M. Patel, A. Benedick, N. H. Amin, M. H. Jones, and A. Miniaci, "Systematic review of autogenous osteochondral transplant outcomes", *Arthroscopy: The Journal of Arthroscopic & Related Surgery*, vol. 31, no. 4, pp. 746–754, 2015.

[30] P. Di Benedetto, M. Citak, D. Kendoff, P. F. O'Loughlin, E. M. Suero, A. D. Pearle, and D. Koulalis, "Arthroscopic mosaicplasty for osteochondral lesions of the knee: computer-assisted navigation versus freehand technique", *Arthroscopy: The Journal of Arthroscopic & Related Surgery*, vol. 28, no. 9, pp. 1290–1296, 2012.

[31] M. Mark, C. Brian, C. Andrew, and S. Jon, *Sports Knee Surgery*, 1st Edition. Saunders, 2008.

[32] D. Koulalis, P. Di Benedetto, M. Citak, P. O'Loughlin, A. D. Pearle, and D. O. Kendoff, "Comparative study of navigated versus freehand osteochondral graft transplantation of the knee", *The American journal of sports medicine*, vol. 37, no. 4, pp. 803–807, 2009.

[33] J. C. Chow, M. E. Hantes, J. B. Houle, and C. G. Zalavras, “Arthroscopic autogenous osteochondral transplantation for treating knee cartilage defects: a 2-to 5-year follow-up study”, *Arthroscopy: The Journal of Arthroscopic & Related Surgery*, vol. 20, no. 7, pp. 681–690, 2004.

[34] M. Marcacci, E. Kon, S. Zaffagnini, F. Iacono, M. P. Neri, A. Vascellari, A. Visani, and A. Russo, “Multiple osteochondral arthroscopic grafting (mosaicplasty) for cartilage defects of the knee: prospective study results at 2-year follow-up”, *Arthroscopy: The Journal of Arthroscopic & Related Surgery*, vol. 21, no. 4, pp. 462–470, 2005.

[35] H Robert, “Chondral repair of the knee joint using mosaicplasty”, *Orthopaedics & Traumatology: Surgery & Research*, vol. 97, no. 4, pp. 418–429, 2011.

[36] A Unnithan, T Jimulia, R Mohammed, and D. Learmonth, “Unique combination of patellofemoral joint arthroplasty with osteochondral autograft transfer system (oats)—a case series of six knees in five patients”, *The Knee*, vol. 15, no. 3, pp. 187–190, 2008.

[37] L. Hangody, G. Kish, Z. Kárpáti, I. Udvarhelyi, I. Szigeti, and M. Bély, “Mosaicplasty for the treatment of articular cartilage defects: application in clinical practice”, *Orthopedics*, vol. 21, no. 7, pp. 751–756, 1998.

[38] R. P. Jakob, T. Franz, E. Gautier, and P. Mainil-Varlet, “Autologous osteochondral grafting in the knee: indication, results, and reflections”, *Clinical orthopaedics and related research*, vol. 401, pp. 170–184, 2002.

[39] M. Thaunat, S. Couchon, J. Lunn, O. Charrois, L. Fallet, and P. Beaufils, “Cartilage thickness matching of selected donor and recipient sites for osteochondral autografting of the medial femoral condyle”, *Knee Surgery, Sports Traumatology, Arthroscopy*, vol. 15, no. 4, pp. 381–386, 2007.

[40] H. Luo, J. Xu, N. H. Binh, S. Liu, C. Zhang, and K. Chen, “A simple calibration procedure for structured light system”, *Optics and Lasers in Engineering*, vol. 57, pp. 6–12, 2014.

[41] Z. Wang, H. Kieu, H. Nguyen, and M. Le, “Digital image correlation in experimental mechanics and image registration in computer vision: similarities, differences and complements”, *Optics and Lasers in Engineering*, vol. 65, pp. 18–27, 2015.

[42] [Online]. Available: `http://www.vision.caltech.edu/bouguetj/calib_doc/`..

[43] A. Milne, D. Chess, J. Johnson, and G. King, “Accuracy of an electromagnetic tracking device: a study of the optimal operating range and metal interference”, *Journal of biomechanics*, vol. 29, no. 6, pp. 791–793, 1996.

[44] G. S. Litynski, “Endoscopic surgery: the history, the pioneers”, *World J. of Surgery*, vol. 23, no. 8, pp. 745–753, 1999.

[45] J. Wickham, “The new surgery.”, *British Medical J. (Clinical Research Ed)*, vol. 295, no. 6613, pp. 1581–1582, 1987.

[46] R. Satava, “3-d vision technology applied to advanced minimally invasive surgery systems”, *Surgical Endoscopy*, vol. 7, no. 5, pp. 429–431, 1993.

[47] K. Cleary and T. M. Peters, "Image-guided interventions: technology review and clinical applications", *Annual Review of Biomedical Engineering*, vol. 12, pp. 119–142, 2010.

[48] Z. Yaniv and K. Cleary, "Image-guided procedures: a review", *Computer Aided Interventions and Medical Robotics*, vol. 3, 2006.

[49] D. Stoyanov, "Stereoscopic scene flow for robotic assisted minimally invasive surgery", in *Proc. of Medical Image Computing and Computer-Assisted Intervention (MICCAI)*, 2012, pp. 479–486.

[50] D. Stoyanov, A. Darzi, and G. Z. Yang, "Dense 3d depth recovery for soft tissue deformation during robotically assisted laparoscopic surgery", in *Proc. of Medical Image Computing and Computer-Assisted Intervention (MICCAI)*, 2004, pp. 41–48.

[51] D. J. Mirota, M. Ishii, and G. D. Hager, "Vision-based navigation in image-guided interventions", *Annual Review of Biomedical Engineering*, vol. 13, pp. 297–319, 2011.

[52] F. Mourgues, F. Devemay, and E. Coste-Maniere, "3d reconstruction of the operating field for image overlay in 3d-endoscopic surgery", in *Proc. of IEEE and ACM Inter. Symp. on Augmented Reality*, 2001, pp. 191–192.

[53] F. Devernay, F. Mourgues, and È. Coste-Manière, "Towards endoscopic augmented reality for robotically assisted minimally invasive cardiac surgery", in *Proc. of IEEE and ACM Inter. Workshop on Augmented Reality*, 2001, pp. 16–20.

[54] C.-H. Wu, Y.-C. Chen, C.-Y. Liu, C.-C. Chang, and Y.-N. Sun, "Automatic extraction and visualization of human inner structures from endoscopic image sequences", in *Proc. of SPIE 5369, Medical Imaging*, 2004, pp. 464–473.

[55] D. Stoyanov, G. P. Mylonas, F. Deligianni, A. Darzi, and G. Z. Yang, "Soft-tissue motion tracking and structure estimation for robotic assisted mis procedures", in *Proc. of Medical Image Computing and Computer-Assisted Intervention (MICCAI)*, 2005, pp. 139–146.

[56] H. Haneishi, T. Ogura, and Y. Miyake, "Profilometry of a gastrointestinal surface by an endoscope with laser beam projection", *Optics Letters*, vol. 19, no. 9, pp. 601–603, 1994.

[57] K. Hasegawa, K. Noda, and Y. Sato, "Electronic endoscope system for shape measurement", in *Proc. of IEEE Inter. Conf. on Pattern Recognition*, 2002, pp. 761–764.

[58] N. T. Clancy, D. Stoyanov, L. Maier-Hein, A. Groch, G.-Z. Yang, and D. S. Elson, "Spectrally encoded fiber-based structured lighting probe for intraoperative 3d imaging", *Biomedical Optics Express*, vol. 2, no. 11, pp. 3119–3128, 2011.

[59] Z. Long and K. Nagamune, "A marching cubes algorithm: application for three-dimensional surface reconstruction based on endoscope and optical fiber", *Information*, vol. 18, no. 4, pp. 1425–1437, 2015.

[60] W. E. Lorensen and H. E. Cline, “Marching cubes: a high resolution 3d surface construction algorithm”, in *ACM siggraph computer graphics*, vol. 21, 1987, pp. 163–169.

[61] G. H. Weber, G. Scheuermann, H. Hagen, and B. Hamann, “Exploring scalar fields using critical isovalues”, in *Proceedings of IEEE Visualization*, 2002, pp. 171–178.

[62] K. Delibasis, G. Matsopoulos, N. Mouravliansky, and K. Nikita, “A novel and efficient implementation of the marching cubes algorithm”, *Computerized Medical Imaging and Graphics*, vol. 25, no. 4, pp. 343–352, 2001.

[63] B. Golosio, G. L. Masala, A. Piccioli, P. Oliva, M. Carpinelli, R. Cataldo, P. Cerello, F. De Carlo, F. Falaschi, M. E. Fantacci, *et al.*, “A novel multi-threshold method for nodule detection in lung ct”, *Medical physics*, vol. 36, no. 8, pp. 3607–3618, 2009.

[64] G. L. Masala, B. Golosio, and P. Oliva, “An improved marching cube algorithm for 3d data segmentation”, *Computer Physics Communications*, vol. 184, no. 3, pp. 777–782, 2013.

[65] T. S. Newman and H. Yi, “A survey of the marching cubes algorithm”, *Computers & Graphics*, vol. 30, no. 5, pp. 854–879, 2006.

[66] T. Toyoshima, “A development of navigation system for normal vector of knee surface in mosaicplasty”, Master thesis, University of Fukui, 2012.

[67] S. Miguet and J.-M. Nicod, “A load-balanced parallel implementation of the marching-cubes algorithm”, in *Proceedings of High performance computing Symp*, vol. 95, 1995, pp. 229–239.

[68] A. Van Gelder and J. Wilhelms, “Topological considerations in isosurface generation”, *ACM Transactions on Graphics (TOG)*, vol. 13, no. 4, pp. 337–375, 1994.

[69] S. L. Chan and E. O. Purisima, “A new tetrahedral tesselation scheme for isosurface generation”, *Computers & Graphics*, vol. 22, no. 1, pp. 83–90, 1998.

[70] C. Montani, R. Scateni, and R. Scopigno, “Discretized marching cubes”, in *Proceedings of IEEE Visualization*, 1994, pp. 281–287.

[71] M. Meissner, U. Hoffmann, and W. Straßer, “Volume rendering using opengl and extensions”, in *Proceedings of IEEE Visualization*, 1999, pp. 207–526.

[72] J. Kniss, S. Premoze, C. Hansen, and D. Ebert, “Interactive translucent volume rendering and procedural modeling”, in *Proceedings of IEEE Visualization*, 2002, pp. 109–116.

[73] P. S. Calhoun, B. S. Kuszyk, D. G. Heath, J. C. Carley, and E. K. Fishman, “Three-dimensional volume rendering of spiral ct data: theory and method 1”, *Radiographics*, vol. 19, no. 3, pp. 745–764, 1999.

[74] C. Lürig, L. Kobbelt, and T. Ertl, "Deformable surfaces for feature based indirect volume rendering", in *Proceedings of the IEEE International Conference on Computer Graphics*, 1998, pp. 752–760.

[75] L. Maier-Hein, P. Mountney, A Bartoli, H Elhawary, D Elson, A. Groch, A Kolb, M. Rodrigues, J Sorger, S. Speidel, and D Stoyanov, "Optical techniques for 3d surface reconstruction in computer-assisted laparoscopic surgery", *Medical Image Analysis*, vol. 17, no. 8, pp. 974–996, 2013.

[76] M. Hu, G. Penney, M. Figl, P. Edwards, F. Bello, R. Casula, D. Rueckert, and D. Hawkes, "Reconstruction of a 3d surface from video that is robust to missing data and outliers: application to minimally invasive surgery using stereo and mono endoscopes", *Medical Image Analysis*, vol. 16, no. 3, pp. 597–611, 2012.

[77] T. D. Brown, D. F. Pope, J. E. Hale, J. A. Buckwalter, and R. A. Brand, "Effects of osteochondral defect size on cartilage contact stress", *J. of orthopaedic research*, vol. 9, no. 4, pp. 559–567, 1991.

[78] L. Hangody, G. K. Rathonyi, Z. Duska, G. Vasarhelyi, P. Fules, and L. Modis, "Autologous osteochondral mosaicplasty", *J Bone Joint Surg Am*, vol. 86, no. suppl 1, pp. 65–72, 2004.

[79] L. Hangody, "Autogenous osteochondral graft technique for replacing knee cartilage defects in dogs", *Orthopedics*, vol. 5, pp. 175–181, 1997.

[80] L Weigelt, S Siebenlist, D Hensler, A. Imhoff, and S Vogt, "Treatment of osteochondral lesions in the elbow: results after autologous osteochondral transplantation", *Archives of orthopaedic and trauma surgery*, vol. 135, no. 5, pp. 627–634, 2015.

[81] N. Iwasaki, H. Kato, J. Ishikawa, T. Masuko, T. Funakoshi, and A. Minami, "Autologous osteochondral mosaicplasty for osteochondritis dissecans of the elbow in teenage athletes", *The J. of Bone & Joint Surgery*, vol. 91, no. 10, pp. 2359–2366, 2009.

[82] P. Ansah, S. Vogt, P. Ueblacker, V. Martinek, K. Woertler, and A. B. Imhoff, "Osteochondral transplantation to treat osteochondral lesions in the elbow", *The J. of Bone & Joint Surgery*, vol. 89, no. 10, pp. 2188–2194, 2007.

[83] T. Yoshizumi, Y. Tsumoto, T. Takiguchi, N. Nagata, Y. Y. Yamamoto, M. Kawashima, T. Ichikawa, M. Nakazawa, N. Yamamoto, and M. Matsui, "Increased level of polyploidy1, a conserved repressor of cyclina2 transcription, controls endoreduplication in arabidopsis", *The Plant Cell*, vol. 18, no. 10, pp. 2452–2468, 2006.

[84] S. G. Pearce, M. B. Hurtig, R. Clarnette, M. Kalra, B. Cowan, and A. Miniaci, "An investigation of 2 techniques for optimizing joint surface congruency using multiple cylindrical osteochondral autografts", *Arthroscopy: The J. of Arthroscopic & Related Surgery*, vol. 17, no. 1, pp. 50–55, 2001.

[85] B. C. Emmerson, S. Görtz, A. A. Jamali, C. Chung, D. Amiel, and W. D. Bugbee, “Fresh osteochondral allografting in the treatment of osteochondritis dissecans of the femoral condyle”, *The American J. of sports medicine*, vol. 35, no. 6, pp. 907–914, 2007.

[86] Z. Long and K. Nagamune, “Underwater surface reconstruction of narrow space by endoscope and optical fiber: application to minimally invasive surgery”, *Poster session presented at: 37th IEEE Int. Conf. of Engineering in Medicine and Biology Society (EMBC), 2015 Aug 29th, Milan, Italy.*,